Piecewise Constant Doppler Algorithm: Performance Analysis, Further Simplification and Motion Compensation

Yijiang Nan, Xiaojing Huang, *Senior Member, IEEE,* and Y. Jay Guo, *Fellow, IEEE*

***Abstract*—The piecewise constant Doppler (PCD) algorithm is a novel radar imaging process recently proposed for the generalized continuous wave synthetic aperture radar (GCW-SAR). This paper presents a detailed theoretical analysis on the PCD algorithm's performance and proposes a further complexity-reduced PCD algorithm with motion compensation (MOCO) suitable for practical applications. Firstly, the difference between conventional SAR imaging and PCD imaging, i.e., the zero-th order versus the first order slant range approximation, is revealed. Exact ambiguity function expressions of the PCD imaging in range and azimuth directions respectively are then derived. An error function of the PCD imaging as compared with the ideal matched filtering method is further defined and shown to be a function of an image quality factor which can be used to quantify the PCD imaging performance. Finally, a faster and more flexible imaging process, called decimated PCD algorithm, is proposed, by which the image azimuth spacing can be easily extended and hence the computational complexity can be significantly reduced. The decimated PCD implementation incorporated with the MOCO is developed for practical GCW-SAR applications and its imaging error lower-bounded by the PCD imaging error function is analyzed accordingly. Simulation and experimental results validate the theoretical analysis of the PCD imaging and show that the decimated PCD algorithm can achieve a high imaging quality at low cost.**

***Index Terms*—Synthetic aperture radar (SAR), continuous wave radar, piecewise constant Doppler (PCD) algorithm, azimuth ambiguity, motion compensation.**

I. Introduction

SYNTHETIC aperture radar (SAR) is a high-resolution remote sensing technique. It can work day and night under all weather conditions by using its own illumination, and has been widely used in many civil and defense applications [1]–[5]. Conventional pulsed SAR repeatedly transmits wideband signal pulses and receives the signals reflected from the observed area during each pulse repetition interval (PRI). The received signals can be viewed as a two-dimensional raw data matrix. One dimension corresponds to the time delay of the backscattered signals, known as the fast time. The other corresponds to the time whenever the radar travels a distance $v\cdot$PRI where v is the radar movement speed, known as the slow time. However, this two-dimensional data structure imposes contradicting requirements on system design, leading to some inherent limitations, e.g., the minimum antenna area constraint [6], [7].

To remove these limitations, some new SAR concepts have been proposed, such as the high resolution and wide swath SAR (HRWS SAR) [8]–[12] and the multiple input and multiple output SAR (MIMO SAR) [13]–[16]. However, using multi-channel transmitters and receivers only improves the spatial resolution and diversity gain. The trade-off in conventional SAR systems remains since the slow time in azimuth is still adopted. The complicated MIMO architecture also leads to some new technical challenges, such as the discontinuous sub-swath [16], which should be synthesized to a continuous wide swath.

Recently, a combination of full-duplex (FD) techniques [17]–[21] and frequency modulated continuous wave SAR (FMCW-SAR) [22]–[25], called generalized continuous wave SAR (GCW-SAR) [26]–[28], has been proposed. With GCW-SAR, the slow time in azimuth is no longer adopted and the final image can be reconstructed from the one-dimensional raw data vector which is obtained by sampling the received backscattered signals after the self-interference cancellation (SIC) at the radio frequency (RF) frontend [19]–[21]. Information about a target in both the range and azimuth dimensions is retrieved jointly with respect to the fast time only and thus the above mentioned restrictions are removed. A novel imaging algorithm suited for the one-dimensional data structure has been proposed based on the piecewise linear approximation of the slant range curve in azimuth [26]. Since the Doppler frequency between the radar and a target in each linear segment becomes a constant, the imaging process is termed piecewise constant Doppler (PCD) algorithm, by which the radar image can be reconstructed recursively in azimuth.

However, the previous work has not tackled the important topic on practical GCW-SAR system design with different performance requirements. The original PCD algorithm itself has a complexity issue since the imaging spacing in azimuth, which is determined by the sampling period of the received signal, is much shorter than the azimuth resolution, leading to many redundant imaging pixels. Furthermore, as a significant step towards practical GCW-SAR application, how to efficiently incorporate motion compensation (MOCO) into the PCD imaging has not been investigated in the previous work. Therefore, the purpose of this paper is to provide a comprehensive theoretical analysis on the PCD imaging algorithm's performance and propose a further simplification incorporated with the MOCO to make the algorithm suitable

This work was supported under the Australian Research Council (ARC) Discovery Project DP 160101693.

Yijiang Nan, Xiaojing Huang and Y. Jay Guo are with the Global Big Data Technologies Center, University of Technology Sydney, NSW, Australia, e-mails: Yijiang.Nan@student.uts.edu.au, Xiaojing.Huang@uts.edu.au, Jay.Guo@uts.edu.au.

for processing real GCW-SAR data. We firstly re-formulate the conventional SAR and PCD imaging processes as the results of the zero-th order and the first order slant range approximations respectively. Based on the slant range of the approximation, the ambiguity functions in range and azimuth respectively for the PCD algorithm are then analytically derived. Afterwards, we analyze the PCD imaging performance in terms of a normalized imaging error as compared with the ideal matched filtering algorithm, which is shown to be a function of an imaging quality factor. This factor quantifies the PCD imaging performance and can be used to guide the GCW-SAR parameter design. In addition, after reviewing the recursive imaging process of the PCD algorithm and further applying the zero-th order approximation on top of the first order approximation to the slant range, we propose a further complexity reduced algorithm, called decimated PCD algorithm, by which the imaging spacing in azimuth can be easily extended, leading to significant reduction of computational cost. As the PCD imaging is based on time-domain correlation with one-dimensional GCW-SAR data structure, spatial sampling does not have to be uniform. With the knowledge of the radar platform navigation, a novel MOCO method is proposed to compensate for any non-ideal radar motion in the GCW-SAR system. The imaging error of the decimated PCD algorithm is also analyzed accordingly.

The remainder of this paper is organized as follows. In Section II, detailed analyses on the ambiguity functions of the PCD algorithm and its imaging error are performed respectively. The decimated PCD algorithm is proposed in Section III with imaging performance and complexity analyses. Section IV and Section V present the simulation and experimental results to validate the imaging error analyses and demonstrate the lower complexity of the decimated PCD algorithm. Finally, conclusions are drawn in Section VI.

II. PCD Algorithm

In this paper, we consider the common stripmap geometry, where the difference between the conventional SAR imaging and PCD imaging can be shown clearly and the PCD imaging analyses can be derived easily. The general stripmap geometry is shown in Fig. 1, where the side-looking radar, at a height h_0, travels along the x-direction with a constant speed v. The incident angle is θ.

For simplicity, only a flat terrain is considered and the time difference between the forward and the back trips is assumed negligible. The demodulated received signal, which is a superposition of reflected echoes from the beam footprint, can be described as

$$s_r(t) = \int\int \sigma(x,y) s(t - \frac{2r(t,x,y)}{c}) e^{-j\frac{4\pi}{\lambda} r(t,x,y)} dxdy \tag{1}$$

where λ is the wavelength of the transmitted RF signal, $\sigma(x,y)$ represents the radar cross section of the terrain being imaged and $s(t)$ is the baseband transmitted signal. The integration is performed over the illuminated area. The instantaneous

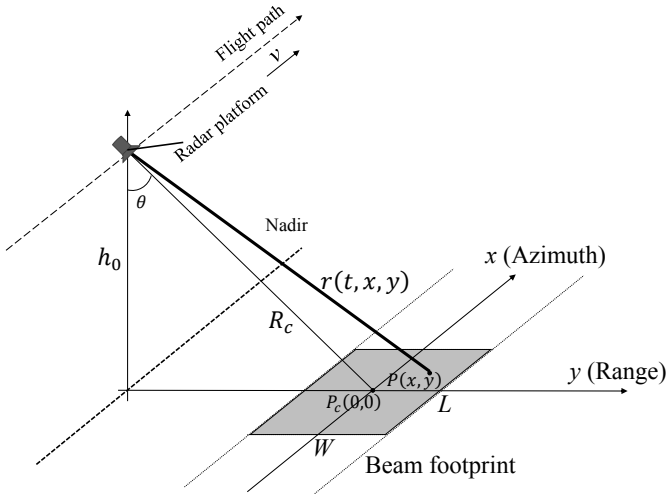

Fig. 1. SAR stripmap geometry.

slant range, i.e., the distance between the radar position and a ground point, is expressed as

$$\begin{aligned} r(t,x,y) &= \sqrt{(R_c sin\theta + y)^2 + (x - vt)^2 + h_0^2} \\ &= \sqrt{R^2(y) + (x-vt)^2} \approx R(y) + \frac{(x-vt)^2}{2R(y)} \end{aligned} \tag{2}$$

which is valid when the condition $|x - vt| \ll R(y) = \sqrt{(R_c sin\theta + y)^2 + h_0^2}$ is satisfied, where R_c is the distance from the radar to the beam footprint center.

Note that the abovementioned quadratic approximation is just used for the ease of analyses. The PCD imaging process can be applied to any form of slant range as long as the radar movement trajectory is known.

A. Imaging Process

Generally speaking, the SAR image reconstruction can be theoretically formulated as a cross-correlation between the received signal and a location dependent reference signal based on the pulse compression principle, known as the ideal matched filtering algorithm. The imaging process of an arbitrary point (x_m, y_n) can be expressed as

$$\begin{aligned} I(x_m, y_n) = \int_{\frac{x_m}{v} - \frac{T}{2}}^{\frac{x_m}{v} + \frac{T}{2}} & s_r(t) s^*(t - \frac{2r(t,x_m,y_n)}{c}) \\ & \cdot e^{j\frac{4\pi}{\lambda} r(t,x_m,y_n)} dt \end{aligned} \tag{3}$$

where the synthetic aperture time is defined as T, the asterisk $*$ indicates complex conjugation, and $s^*(t - \frac{2r(t,x_m,y_n)}{c}) e^{j\frac{4\pi}{\lambda} r(t,x_m,y_n)}$ is the location dependent reference signal for the point (x_m, y_n).

In conventional SAR, the transmission and reception are repeated every PRI, and the slant range of point (x_m, y_n) in each PRI is assumed to be constant, thus forming the zero-th order approximation of $r(t, x_m, y_n)$ shown in Fig. 2 (a) and described as

$$\widetilde{r}_0(t, x_m, y_n) = r(\tau_q, x_m, y_n), t \in [\tau_q, \tau_q + PRI) \tag{4}$$

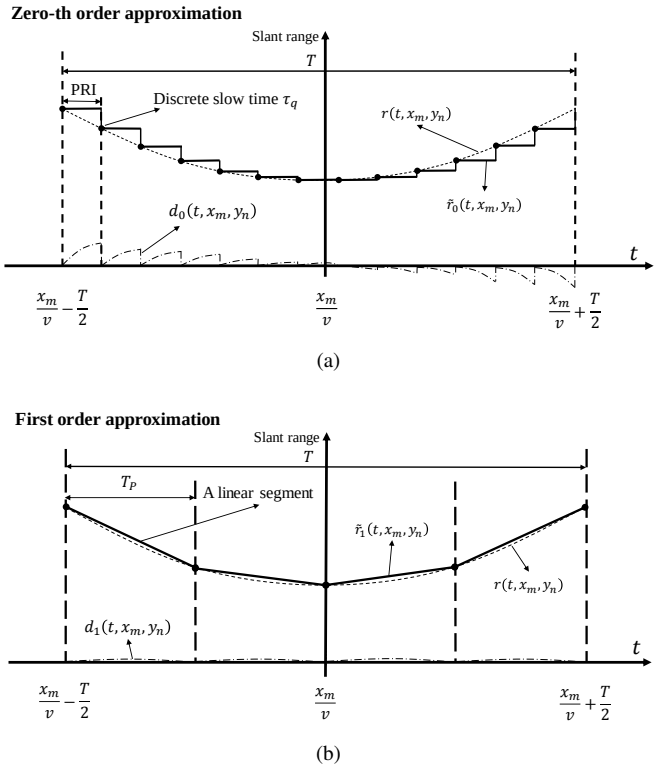

Fig. 2. Slant range approximations in conventional SAR imaging and PCD imaging: (a) conventional SAR imaging; (b) PCD imaging.

where $\tau_q = q \cdot PRI + x_m/v - T/2$, $q = 0, 1, ..., [T/PRI]-1$, indicates the start of each PRI and $[T/PRI]$ is the number of PRIs over T. The conventional SAR imaging process can be expressed as

$$\begin{aligned} & I_0(x_m, y_n) \\ &= \int_{\frac{x_m}{v}-\frac{T}{2}}^{\frac{x_m}{v}+\frac{T}{2}} s_r(t) s^*(t - \frac{2\widetilde{r}_0(t, x_m, y_n)}{c}) e^{j\frac{4\pi}{\lambda}\widetilde{r}_0(t,x_m,y_n)} dt \\ &= \sum_{q=0}^{[T/PRI]-1} \int_{q\cdot PRI+\frac{x_m}{v}-\frac{T}{2}}^{(q+1)\cdot PRI+\frac{x_m}{v}-\frac{T}{2}} s_r(t) s^*(t - \frac{2r(\tau_q, x_m, y_n)}{c}) dt \\ & \cdot e^{j\frac{4\pi}{\lambda}r(\tau_q,x_m,y_n)} \end{aligned} \tag{5}$$

where t, the fast time, describes the time delay of the received signals during each PRI, whereas τ_q, the slow time, describes the discrete time instants whenever the radar travels over a PRI. Therefore, the cross-correlation can be manipulated by independent range and azimuth compressions. This conventional operation enables fast Fourier transform (FFT) based imaging algorithms with low computational complexity, e.g., the range Doppler algorithm [7].

The error caused by the zero-th order approximation is presented as the black dash-dot line in Fig. 2 (a) and can be described as

$$\begin{aligned} & d_0(t, x_m, y_n) = \widetilde{r}_0(t, x_m, y_n) - r(t, x_m, y_n) \\ & \approx \frac{(x_m - v\tau_q)^2 - (x_m - vt)^2}{2R(y_n)} \\ & = \frac{-v^2t^2 + 2x_m vt + v^2\tau_q^2 - 2x_m v\tau_q}{2R(y_n)}, t \in [\tau_q, \tau_q + PRI) \end{aligned} \tag{6}$$

which indicates that the error in each PRI is different from one another.

The zero-th order approximation leads to some intrinsic limitations in conventional SARs. Firstly, the contradiction between range swath and azimuth resolution is inevitable. To satisfy the azimuth sampling requirement with high Doppler frequency bandwidth, the PRI needs to be short, but a short PRI leads to a narrow range swath. Secondly, the continuous motion within a sweep in FMCW-SAR leads to a range walk term and additional range-azimuth coupling which have to be compensated before the image focusing [24]. In addition, range cell migration is also necessary due to the slow time sampling, which complicates the imaging process [7].

With GCW-SAR, the transmission and reception are conducted at the same time, generating a one-dimensional raw data structure without PRI [26]. Based on the PCD imaging principle, GCW-SAR adopts the first order approximation of the slant range which is composed of P linear segments linked end to end, as shown in Fig. 2 (b). Note that $r(t + \frac{x_m}{v}, x_m, y_n) = r(t, 0, y_n)$ is valid in the flat terrain case. Assuming that the length of each segment is $T_P = T/P$ and the p-th segment starts from $t_p = p \cdot T_P - \frac{T}{2}, p = 0, 1, 2, ...P-1$, the corresponding linear approximated slant range can be expressed as

$$\begin{aligned} & \widetilde{r}_1(t, x_m, y_n) \\ & = \frac{r(t_{p+1} + \frac{x_m}{v}, x_m, y_n) - r(t_p + \frac{x_m}{v}, x_m, y_n)}{(t_{p+1} - t_p)} \\ & \cdot (t - t_p - \frac{x_m}{v}) + r(t_p + \frac{x_m}{v}, x_m, y_n) \\ & = \frac{r(t_{p+1}, 0, y_n) - r(t_p, 0, y_n)}{(t_{p+1} - t_p)} (t - t_p - \frac{x_m}{v}) \\ & + r(t_p, 0, y_n) \\ & = -\frac{\lambda}{2} f_{D_p}(y_n)(t - t_p - \frac{x_m}{v}) + r(t_p, 0, y_n) \\ & , t \in [t_p + \frac{x_m}{v}, t_{p+1} + \frac{x_m}{v}) \end{aligned} \tag{7}$$

where $f_{D_p}(y_n) = -\frac{2}{\lambda}\frac{r(t_{p+1},0,y_n) - r(t_p,0,y_n)}{t_{p+1}-t_p}$ is the constant Doppler frequency for the p-th segment. Thus, the PCD imaging process for the point (x_m, y_n) can be described as

$$\begin{aligned} & I_1(x_m, y_n) \\ &= \int_{\frac{x_m}{v}-\frac{T}{2}}^{\frac{x_m}{v}+\frac{T}{2}} s_r(t) s^*(t - \frac{2\widetilde{r}_1(t, x_m, y_n)}{c}) e^{j\frac{4\pi}{\lambda}\widetilde{r}_1(t,x_m,y_n)} dt \\ &= \sum_{p=0}^{P-1} \int_{p\cdot T_P+\frac{x_m}{v}-\frac{T}{2}}^{(p+1)\cdot T_P+\frac{x_m}{v}-\frac{T}{2}} s_r(t) s^*(t - \frac{2\widetilde{r}_1(t, x_m, y_n)}{c}) \\ & \cdot e^{-j2\pi f_{D_p}(y_n)(t-t_p-\frac{x_m}{v})+j\frac{4\pi}{\lambda}r(t_p,0,y_n)} dt. \end{aligned} \tag{8}$$

With the linear approximation, two adjacent image points $I_1(x_m, y_n)$ and $I_1(x_m + \Delta x, y_n)$ spaced by Δx are mainly different by a constant phase shift, $e^{j2\pi f_{D_p}(y_n)\frac{\Delta x}{v}}$, for the p-th segment in addition to a minor adjustment of the integration interval. Therefore, the images can be reconstructed recursively in azimuth without any involvement of the slow time and hence the inherent limitations in conventional SARs are removed.

The error caused by the first order approximation is shown in Fig. 2 (b) plotted with the black dash-dot line. From (2) and (7), it can be expressed as

$$\begin{aligned}
&d_1(t, x_m, y_n) = \widetilde{r}_1(t, x_m, y_n) - r(t, x_m, y_n) \\
&= -\frac{\lambda}{2} f_{D_p}(y_n)(t - t_p - \frac{x_m}{v}) + r(t_p, 0, y_n) - r(t, x_m, y_n) \\
&\approx \frac{R(y_n) + \frac{v^2 t_{p+1}^2}{2R(y_n)} - R(y_n) - \frac{v^2 t_p^2}{2R(y_n)}}{t_{p+1} - t_p}(t - t_p - \frac{x_m}{v}) \\
&+ R(y_n) + \frac{v^2 t_p^2}{2R(y_n)} - R(y_n) - \frac{(x_m - vt)^2}{2R(y_n)} \\
&= -\frac{(x_m - vt)^2 + v(t_{p+1} + t_p)(x_m - vt) + v^2 t_p t_{p+1}}{2R(y_n)} \\
&, t \in [t_p + \frac{x_m}{v}, t_{p+1} + \frac{x_m}{v}).
\end{aligned} \tag{9}$$

It is also interesting to see that

$$\begin{aligned}
&d_1(t + T_P, x_m, y_n) \\
&= -\frac{1}{2R(y_n)}((x_m - v(t + T_P))^2 + v(t_{p+1} + t_p + 2T_P) \\
&\cdot (x_m - v(t + T_P)) + v^2(t_p + T_P)(t_{p+1} + T_P)) \\
&= -\frac{1}{2R(y_n)}((x_m - vt)^2 - 2(x_m - vt)vT_P + v^2 T_P^2 \\
&+ v(t_{p+1} + t_p)(x_m - vt) - 2v^2 T_P^2 + 2(x_m - vt)vT_P \\
&- v^2 T_P(t_p + t_{p+1}) + v^2 t_p t_{p+1} + v^2 T_P(t_p + t_{p+1}) + v^2 T_P^2) \\
&= d_1(t, x_m, y_n), t \in [t_p + \frac{x_m}{v}, t_{p+1} + \frac{x_m}{v})
\end{aligned} \tag{10}$$

which demonstrates that $d_1(t, x_m, y_n)$ is a periodic function with period T_P.

As seen from Fig. 2, the error is largely reduced with linear approximation, and thus the PCD algorithm can perform well even with a small number of segments P. Moreover, the aforementioned intrinsic limitations caused by the slow time sampling are eliminated in the PCD algorithm.

B. PCD Ambiguity Function

For a given one-point SAR target, the ambiguity functions of the PCD algorithm can be derived as follows. Assuming that the target is located at the origin $(0, 0)$, the received signal can be expressed as $s_r(t) = \sigma(0,0)s(t - \frac{2r(t,0,0)}{c})e^{-j\frac{4\pi}{\lambda}r(t,0,0)}$ and the PCD image can be expressed as

$$\begin{aligned}
&I_1(x_m, y_n) \\
&= \int_{\frac{x_m}{v} + \frac{T}{2}}^{\frac{x_m}{v} - \frac{T}{2}} \sigma(0,0)s(t - \frac{2r(t,0,0)}{c}) \\
&\cdot s^*(t - \frac{2\widetilde{r}_1(t, x_m, y_n)}{c}) e^{j\frac{4\pi}{\lambda}(\widetilde{r}_1(t, x_m, y_n) - r(t,0,0))} dt.
\end{aligned} \tag{11}$$

For simplicity, we consider the two cases $I_1(0, y_n)$ and $I_1(x_m, 0)$ respectively. The first one represents the image in range direction and the second one in azimuth direction.

1) Imaging in Range: When $x_m = 0$, we have

$$\begin{aligned}
&\widetilde{r}_1(t, 0, y_n) - r(t, 0, 0) \\
&= -\frac{\lambda}{2} f_{D_p}(y_n)(t - t_p) + r(t_p, 0, y_n) - r(t, 0, 0) \\
&\approx \frac{v^2(t_{p+1} + t_p)}{2R(y_n)}(t - t_p) + R(y_n) + \frac{v^2 t_p^2}{2R(y_n)} - R_c - \frac{v^2 t^2}{2R_c} \\
&\approx R(y_n) - R_c
\end{aligned} \tag{12}$$

since the slant range $R(y_n)$ is much larger than the length of segment $T_P v$. Assuming that $s(t)$ satisfies the requirement of the transmitted waveform in GCW-SAR [26], i.e., it is any normalized low-pass baseband signal with constant energy spectrum in its bandwidth B, Eq. (11) can then be simplified as

$$\begin{aligned}
&I_1(0, y_n) \\
&\approx e^{j\frac{4\pi}{\lambda}(R(y_n) - R_c)} \int_{-\frac{T}{2}}^{\frac{T}{2}} \sigma(0,0)s(t - \frac{2r(t,0,0)}{c}) \\
&\cdot s^*(t - \frac{2\widetilde{r}_1(t,0,y_n)}{c}) dt \\
&\approx e^{j\frac{4\pi}{\lambda}(R(y_n) - R_c)} \int_{-\frac{T}{2}}^{\frac{T}{2}} \sigma(0,0)s(t - \frac{2R_c - 2R(y_n)}{c}) s^*(t) dt \\
&\approx \sigma(0,0)e^{j\frac{4\pi}{\lambda}(R(y_n) - R_c)} sinc(\frac{2B}{c}(R(y_n) - R_c))
\end{aligned} \tag{13}$$

where $sinc(t)$ is the sinc function defined by $sin(\pi t)/\pi t$. Consequently, PCD algorithm has a negligible loss on SAR imaging performance in range direction.

2) Imaging in Azimuth: When $y_n = 0$, Eq. (11) becomes

$$\begin{aligned}
&I_1(x_m, 0) \\
&= \int_{\frac{x_m}{v} - \frac{T}{2}}^{\frac{x_m}{v} + \frac{T}{2}} \sigma(0,0)s(t - \frac{2r(t,0,0)}{c}) \\
&\cdot s^*(t - \frac{2\widetilde{r}_1(t, x_m, 0)}{c}) e^{j\frac{4\pi}{\lambda}(\widetilde{r}_1(t, x_m, 0) - r(t,0,0))} dt \\
&= \int_{-\frac{T}{2}}^{\frac{T}{2}} \sigma(0,0)s(t + \frac{x_m}{v} - \frac{2r(t + \frac{x_m}{v}, 0, 0)}{c}) \\
&\cdot s^*(t + \frac{x_m}{v} - \frac{2\widetilde{r}_1(t + \frac{x_m}{v}, \frac{x_m}{v}, 0)}{c}) \\
&\cdot e^{j\frac{4\pi}{\lambda}(\widetilde{r}_1(t + \frac{x_m}{v}, x_m, 0) - r(t + \frac{x_m}{v}, 0, 0))}.
\end{aligned} \tag{14}$$

Substituting $r(t + \frac{x_m}{v}, \frac{x_m}{v}, 0) = r(t, 0, 0)$, $\widetilde{r}_1(t + \frac{x_m}{v}, \frac{x_m}{v}, 0) = \widetilde{r}_1(t, 0, 0)$, $d_1(t, 0, 0) = \widetilde{r}_1(t, 0, 0) - r(t, 0, 0)$ and (2) into (14),

$$\begin{aligned}
&\frac{d|W(x)|}{dx} \\
&= \sqrt{\frac{L_aP^2}{2\pi L}} \frac{1}{2\sqrt{(C(\sqrt{\frac{2\pi x^2}{LL_a}}+\sqrt{\frac{\pi L}{2L_aP^2}})-C(\sqrt{\frac{2\pi x^2}{LL_a}}-\sqrt{\frac{\pi L}{2L_aP^2}}))^2+(S(\sqrt{\frac{2\pi x^2}{LL_a}}-\sqrt{\frac{\pi L}{2L_aP^2}})-S(\sqrt{\frac{2\pi x^2}{LL_a}}+\sqrt{\frac{\pi L}{2L_aP^2}}))^2}} \\
&\cdot \Bigg(2\Big(C(\sqrt{\frac{2\pi x^2}{LL_a}}+\sqrt{\frac{\pi L}{2L_aP^2}})-C(\sqrt{\frac{2\pi x^2}{LL_a}}-\sqrt{\frac{\pi L}{2L_aP^2}})\Big)\Big(cos(\frac{2\pi}{LL_a}(x+\frac{L}{2P})^2)-cos(\frac{2\pi}{LL_a}(x-\frac{L}{2P})^2)\Big) \\
&+2\Big(S(\sqrt{\frac{2\pi x^2}{LL_a}}-\sqrt{\frac{\pi L}{2L_aP^2}})-S(\sqrt{\frac{2\pi x^2}{LL_a}}+\sqrt{\frac{\pi L}{2L_aP^2}})\Big)\Big(sin(\frac{2\pi}{LL_a}(x-\frac{L}{2P})^2)-sin(\frac{2\pi}{LL_a}(x+\frac{L}{2P})^2)\Big)\Bigg)
\end{aligned} \tag{18}$$

$$\begin{aligned}
\epsilon^2 &= \frac{\int_{-\infty}^{\infty}|\sigma(0,0)e^{-j\frac{2\pi x_m^2}{\lambda R_c}}\frac{1}{T}\int_{-\infty}^{\infty}rect(\frac{t}{T})e^{j\frac{4\pi}{\lambda}d_1(t,0,0)}e^{-j2\pi\Omega t}dt-\sigma(0,0)e^{-j\frac{2\pi x_m^2}{\lambda R_c}}\frac{1}{T}\int_{-\infty}^{\infty}rect(\frac{t}{T})e^{-j2\pi\Omega t}dt|^2\cdot\frac{\lambda R_c}{2v}d\Omega}{\int_{-\infty}^{\infty}|\sigma(0,0)e^{-j\frac{2\pi x_m^2}{\lambda R_c}}\frac{1}{T}\int_{-\infty}^{\infty}rect(\frac{t}{T})e^{-j2\pi\Omega t}dt|^2\cdot\frac{\lambda R_c}{2v}d\Omega} \\
&= \frac{\int_{-\infty}^{\infty}|\int_{-\infty}^{\infty}rect(\frac{t}{T})(e^{j\frac{4\pi}{\lambda}d_1(t,0,0)}-1)e^{-j2\pi\Omega t}dt|^2d\Omega}{\int_{-\infty}^{\infty}|\int_{-\infty}^{\infty}rect(\frac{t}{T})e^{-j2\pi\Omega t}dt|^2d\Omega}
\end{aligned} \tag{21}$$

$I_1(x_m,0)$ can be simplified as

$$\begin{aligned}
&I_1(x_m,0) \\
&= \int_{-\frac{T}{2}}^{\frac{T}{2}}\sigma(0,0)s(t+\frac{x_m}{v}-\frac{2r(t+\frac{x_m}{v},0,0)}{c}) \\
&\cdot s^*(t+\frac{x_m}{v}-\frac{2\widetilde{r}_1(t,0,0)}{c})e^{j\frac{4\pi}{\lambda}(\widetilde{r}_1(t,0,0)-r(t,0,0))} \\
&\cdot e^{j\frac{4\pi}{\lambda}(r(t,0,0)-r(t+\frac{x_m}{v},0,0))}dt \\
&= \sigma(0,0)e^{-j\frac{2\pi x_m^2}{\lambda R_c}}\int_{-\frac{T}{2}}^{\frac{T}{2}}s(t+\frac{x_m}{v}-\frac{2r(t+\frac{x_m}{v},0,0)}{c}) \\
&\cdot s^*(t+\frac{x_m}{v}-\frac{2\widetilde{r}_1(t,0,0)}{c})e^{j\frac{4\pi}{\lambda}d_1(t,0,0)}e^{-j2\pi\frac{2vx_m}{\lambda R_c}t}dt.
\end{aligned} \tag{15}$$

Further assuming that $s(t)$ is a phase only signal, i.e., $s(t)=\frac{1}{\sqrt{T}}e^{j\phi(t)}$, where $\phi(t)$ is any phase function, and approximating $s(t-\frac{2r(t+\frac{x_m}{v},,0)}{c})$ as $s(t-\frac{2\widetilde{r}(t,0,0)}{c})$ when the condition $|x_m-vt|<<R(y)$ is satisfied, the image $I_1(x_m,0)$ can be further simplified as

$$\begin{aligned}
&I_1(x_m,0) \\
&= \sigma(0,0)e^{-j\frac{2\pi x_m^2}{\lambda R_c}}\frac{1}{T}\int_{-\frac{T}{2}}^{\frac{T}{2}}e^{j\frac{4\pi}{\lambda}d_1(t,0,0)}e^{-j2\pi\frac{2vx_m}{\lambda R_c}t}dt \\
&= \sigma(0,0)e^{-j\frac{2\pi x_m^2}{LL_a}}\sum_{i=-\infty}^{\infty}W(iP\frac{L_a}{2}) \\
&\cdot sinc(\frac{2}{L_a}(x_m-iP\frac{L_a}{2}))
\end{aligned} \tag{16}$$

where $L=vT\approx\frac{\lambda}{L_a}R_c$ is defined as the synthetic aperture and L_a the antenna aperture in azimuth. The detailed derivation of (16) is provided in Appendix A. Clearly, $I_1(x_m,0)$ is a weighted sum of sinc functions with equal spacing $P\frac{L_a}{2}$ in azimuth. The weight function $W(x)$ is defined as (see Appendix B)

$$\begin{aligned}
W(x) &= \frac{1}{T_P}\int_{-\frac{T_P}{2}}^{\frac{T_P}{2}}e^{j\frac{4\pi}{\lambda}d_1(t,0,0)}e^{-j2\pi\frac{2vx}{\lambda R_c}t}dt \\
&= \sqrt{\frac{L_aP^2}{2\pi L}}e^{j\frac{\pi L}{2L_aP^2}}e^{j\frac{2\pi x^2}{LL_a}}\Big(C(\sqrt{\frac{2\pi x^2}{LL_a}}+\sqrt{\frac{\pi L}{2L_aP^2}}) \\
&- C(\sqrt{\frac{2\pi x^2}{LL_a}}-\sqrt{\frac{\pi L}{2L_aP^2}})+jS(\sqrt{\frac{2\pi x^2}{LL_a}}-\sqrt{\frac{\pi L}{2L_aP^2}}) \\
&- jS(\sqrt{\frac{2\pi x^2}{LL_a}}+\sqrt{\frac{\pi L}{2L_aP^2}})\Big)
\end{aligned} \tag{17}$$

where $S(x)$ and $C(x)$ are the Fresnel integrals [29] also defined in Appendix B.

The first derivative of $|W(x)|$ can be found as shown in (18). Note that $\frac{d|W(x)|}{dx}=0$ when $\frac{2\pi}{LL_a}(x-\frac{L}{2P})^2-\frac{2\pi}{LL_a}(x+\frac{L}{2P})^2=i\cdot 2\pi$, for $i=0,\pm1,\pm2,...$, thus $x=i\cdot P\frac{L_a}{2}$ are the extremums of $|W(x)|$. Interestingly, the sinc function $sinc(\frac{2}{L_a}(x_m-iP\frac{L_a}{2}))$ are also located at these extremum points and we will show later in the simulation results that they are actually the minimum points of $|W(x)|$ except for $i=0$.

C. PCD Imaging Performance

The normalized PCD imaging error as compared with the ideal matched filtering method can be evaluated as

$$\epsilon^2 = \frac{\int_{-\infty}^{\infty}|I_1(x_m,0)-I(x_m,0)|^2dx_m}{\int_{-\infty}^{\infty}|I(x_m,0)|^2dx_m} \tag{19}$$

where $I(x_m,0)$ is the ideal image expressed as

$$\begin{aligned} I(x_m,0) &= \sigma(0,0)\int_{\frac{x_m}{v}-\frac{T}{2}}^{\frac{x_m}{v}+\frac{T}{2}} s(t-\frac{2r(t,0,0)}{c}) \\ &\cdot s^*(t-\frac{2r(t,x_m,0)}{c})e^{j\frac{4\pi}{\lambda}(r(t,x_m,0)-r(t,0,0))}dt \\ &= \sigma(0,0)\int_{-\frac{T}{2}}^{\frac{T}{2}} s(t+\frac{x_m}{v}-\frac{2r(t+\frac{x_m}{v},0,0)}{c}) \\ &\cdot s^*(t+\frac{x_m}{v}-\frac{2r(t,0,0)}{c})e^{j\frac{4\pi}{\lambda}(r(t,0,0)-r(t+\frac{x_m}{v},0,0))}dt \\ &\approx \sigma(0,0)e^{-j\frac{2\pi x_m^2}{\lambda R_c}}\frac{1}{T}\int_{-\infty}^{\infty} rect(\frac{t}{T})e^{-j2\pi\frac{2vx_m}{\lambda R_c}t}dt \end{aligned} \tag{20}$$

with the same assumptions and methods used in the derivation of (16). Denoting $\frac{2vx_m}{\lambda R_c}$ and substituting (36) in Appendix A and (20) into (19), ϵ^2 can be further derived as (21). According to Parseval's Theorem, the power in frequency domain is equal to that in time domain. Therefore, Eq. (21) can be further simplified as

$$\begin{aligned} \epsilon^2 &= \frac{\int_{-\infty}^{\infty}|rect(\frac{t}{T})(e^{j\frac{4\pi}{\lambda}d_1(t,0,0)}-1)|^2dt}{\int_{-\infty}^{\infty}|rect(\frac{t}{T})|^2dt} \\ &= \frac{\int_{-\frac{T_P}{2}}^{\frac{T_P}{2}}|e^{j\frac{4\pi}{\lambda}d_1(t,0,0)}-1|^2dt}{\int_{-\frac{T_P}{2}}^{\frac{T_P}{2}}|1|^2dt} \\ &= \frac{1}{T_P}\int_{-\frac{T_P}{2}}^{\frac{T_P}{2}}(e^{j\frac{4\pi}{\lambda}d_1(t,0,0)}-1)(e^{-j\frac{4\pi}{\lambda}d_1(t,0,0)}-1)dt \\ &= 2-\frac{1}{T_P}\int_{-\frac{T_P}{2}}^{\frac{T_P}{2}}e^{j\frac{4\pi}{\lambda}d_1(t,0,0)}dt-\frac{1}{T_P}\int_{-\frac{T_P}{2}}^{\frac{T_P}{2}}e^{-j\frac{4\pi}{\lambda}d_1(t,0,0)}dt \\ &= 2-W(0)-W^*(0) = 2-2Re\{W(0)\} \end{aligned} \tag{22}$$

where $Re\{W(0)\}$ is the real part of $W(0)$. Since the Fresnel integrals $C(.)$ and $S(.)$ are odd functions, $W(0)$ can be derived from (17) as

$$\begin{aligned} W(0) &= \sqrt{\frac{L_aP^2}{2\pi L}}e^{j\frac{\pi L}{2L_aP^2}}\Big(C(\sqrt{\frac{\pi L}{2L_aP^2}})-C(-\sqrt{\frac{\pi L}{2L_aP^2}}) \\ &+ jS(-\sqrt{\frac{\pi L}{2L_aP^2}})-jS(\sqrt{\frac{\pi L}{2L_aP^2}})\Big) \\ &= \sqrt{\frac{2Q}{\pi}}e^{j\frac{\pi}{2Q}}\Big(C(\sqrt{\frac{\pi}{2Q}})-jS(\sqrt{\frac{\pi}{2Q}})\Big) \end{aligned} \tag{23}$$

where $Q=\frac{L_aP^2}{L}$ is defined as the image quality factor. From (22) and (23) we see that the normalized PCD imaging error is a function of Q. The error function curve shown in Fig. 3 indicates that the PCD imaging performs better as Q increases.

Therefore, for a given quality factor, the GCW-SAR parameters L_a, L, and P can be selected appropriately to satisfy the required PCD imaging performance.

III. Decimated PCD Algorithm

With the PCD algorithm described in [26], the image pixels in azimuth direction are reconstructed recursively with

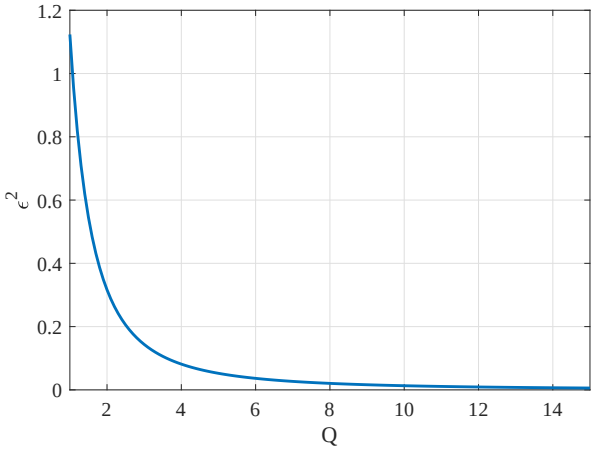

Fig. 3. Normalized PCD imaging error as a function of Q.

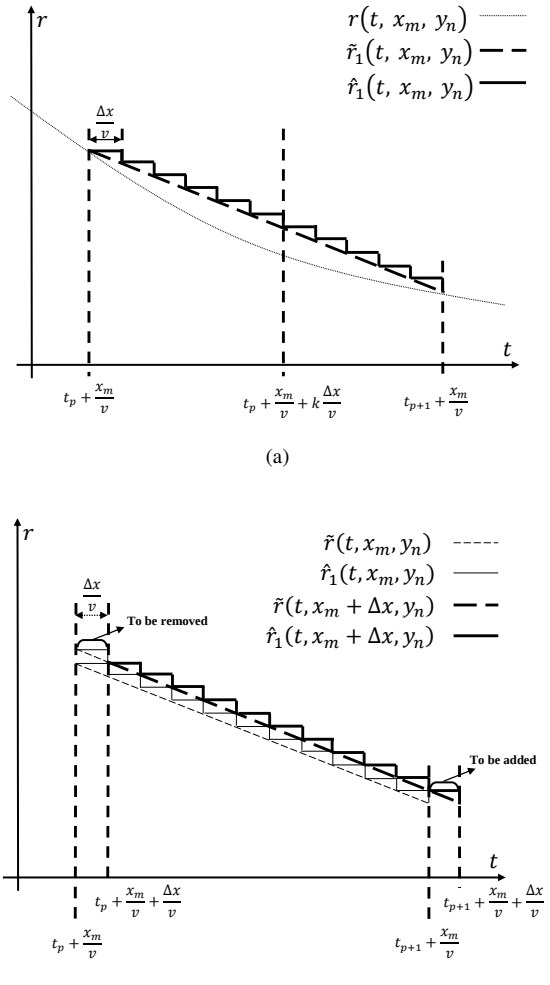

Fig. 4. Decimated PCD imaging: (a) slant range approximation; (b) recursive imaging process from $\frac{x_m}{v}$ to $\frac{x_m+\Delta x}{v}$.

a spacing equivalent to the signal sampling period T_s, i.e., $\Delta x = T_s v$. Since the azimuth sampling rate is much larger than the Doppler frequency bandwidth, the image spacing in azimuth direction is much shorter than the azimuth resolution,

leading to a large amount of redundant image points and hence significant computational cost. In addition, the MOCO also needs to be considered for practical GCW-SAR application. In this section, we revisit the recursive process in PCD algorithm and design a faster algorithm incorporated with MOCO with significantly reduced computational complexity.

A. PCD Recursive Process

In the PCD algorithm, the range curve has been divided into P linear segments. Thus, the image $I_1(x_m, y_n)$ can be computed as a sum of the integrals over all the respective segments, i.e., $I_1(x_m, y_n) = \sum_{p=0}^{P-1} I_1^{(p)}(x_m, y_n)$, where the integral over the p-th segment can be expressed as

$$\begin{aligned} &I_1^{(p)}(x_m, y_n) \\ &= \int_{\frac{x_m}{v}+t_p}^{\frac{x_m}{v}+t_{p+1}} s_r(t) s^*(t - \frac{2\widetilde{r}_1(t, x_m, y_n)}{c}) \\ &\cdot e^{j\frac{4\pi}{\lambda}\widetilde{r}_1(t,x_m,y_n)} dt. \end{aligned} \tag{24}$$

If the transmitted signal satisfies the condition $s^*(t + \frac{x_m}{v} - \frac{2r(t,\Delta x,y_n)}{c}) \approx s^*(t + \frac{x_m}{v} - \frac{2r(t,0,y_n)}{c})$, from (7) and $r(t + \frac{x_m}{v}, x_m, y_n) = r(t, 0, y_n)$, the image $I_1^{(p)}(x_m + \Delta x, y_n)$ at the next azimuth point can be expressed as

$$\begin{aligned} &I_1^{(p)}(x_m + \Delta x, y_n) \\ &= \int_{\frac{x_m}{v}+\frac{\Delta x}{v}+t_p}^{\frac{x_m}{v}+\frac{\Delta x}{v}+t_{p+1}} s_r(t) s^*(t - \frac{2\widetilde{r}_1(t, x_m + \Delta x, y_n)}{c}) \\ &\cdot e^{j\frac{4\pi}{\lambda}\widetilde{r}_1(t,x_m+\Delta x,y_n)} dt \\ &= \int_{\frac{\Delta x}{v}+t_p}^{\frac{\Delta x}{v}+t_{p+1}} s_r(t + \frac{x_m}{v}) s^*(t + \frac{x_m}{v} - \frac{2\widetilde{r}_1(t, \Delta x, y_n)}{c}) \\ &\cdot e^{j\frac{4\pi}{\lambda}\widetilde{r}_1(t,\Delta x,y_n)} dt \\ &\approx \int_{t_p}^{t_{p+1}} s_r(t + \frac{x_m}{v}) s^*(t + \frac{x_m}{v} - \frac{2\widetilde{r}_1(t, 0, y_n)}{c}) \\ &\cdot e^{j\frac{4\pi}{\lambda}(-\frac{\lambda}{2}f_{D_p}(y_n)(t-t_p)+r(t_p,0,y_n))} e^{j2\pi f_{D_p}(y_n)\frac{\Delta x}{v}} dt \\ &- \int_{t_p}^{\frac{\Delta x}{v}+t_p} s_r(t + \frac{x_m}{v}) s^*(t + \frac{x_m}{v} - \frac{2\widetilde{r}_1(t, \Delta x, y_n)}{c}) \\ &\cdot e^{j\frac{4\pi}{\lambda}\widetilde{r}_1(t,\Delta x,y_n)} dt \\ &+ \int_{t_{p+1}}^{\frac{\Delta x}{v}+t_{p+1}} s_r(t + \frac{x_m}{v}) s^*(t + \frac{x_m}{v} - \frac{2\widetilde{r}_1(t, \Delta x, y_n)}{c}) \\ &\cdot e^{j\frac{4\pi}{\lambda}\widetilde{r}_1(t,\Delta x,y_n)} dt \\ &= I_1^{(p)}(x_m, y_n) e^{j2\pi f_{D_p}(y_n)\frac{\Delta x}{v}} \\ &- \int_{t_p}^{\frac{\Delta x}{v}+t_p} s_r(t + \frac{x_m}{v}) s^*(t + \frac{x_m}{v} - \frac{2\widetilde{r}_1(t, \Delta x, y_n)}{c}) \\ &\cdot e^{j\frac{4\pi}{\lambda}\widetilde{r}_1(t,\Delta x,y_n)} dt \\ &+ \int_{t_{p+1}}^{\frac{\Delta x}{v}+t_{p+1}} s_r(t + \frac{x_m}{v}) s^*(t + \frac{x_m}{v} - \frac{2\widetilde{r}_1(t, \Delta x, y_n)}{c}) \\ &\cdot e^{j\frac{4\pi}{\lambda}\widetilde{r}_1(t,\Delta x,y_n)} dt. \end{aligned} \tag{25}$$

From (25) the three steps of the recursive imaging process in the PCD algorithm can be described as: 1) compensating the Doppler frequency shift from the previous image point; 2) removing the integral over time interval $[\frac{x_m}{v} + t_p, \frac{x_m}{v} + \frac{\Delta x}{v} + t_p)$; and 3) adding the integral over time interval $[\frac{x_m}{v} + t_{p+1}, \frac{x_m}{v} + \frac{\Delta x}{v} + t_{p+1})$.

B. Decimated PCD Principle

To remove the redundant imaging pixels, the imaging spacing Δx can be extended corresponding to multiple sampling periods, resulting in a decimated PCD algorithm. We further take the zero-th order approximation on top of the linear segments of the slant range as shown in Fig. 4 (a). The approximated slant range curves $\widetilde{r}_1(t, x_m, y_n)$ and $\hat{r}_1(t, x_m, y_n)$ during $[t_p, t_{p+1})$ for PCD and decimated PCD algorithms are shown respectively using the dash and solid lines. Just as in the conventional SAR imaging, the azimuth image spacing Δx can be as large as that corresponding to a PRI.

The recursive imaging process of the decimated PCD algorithm is shown in Fig. 4 (b). Note that after the further zero-th order slant range approximation the Doppler frequency shift remains the same since $\hat{r}_1(t, x_m, y_n) - \hat{r}_1(t, x_m + \Delta x, y_n) = \widetilde{r}_1(t, x_m, y_n) - \widetilde{r}_1(t, x_m + \Delta x, y_n)$, and that the slant range can be considered as a constant over the integration interval $[0, \Delta x/v)$, i.e., $\hat{r}_1(t + t_p, \Delta x, y_n) = r(t_p, \Delta x, y_n)$. Therefore, from (25), the p-th segment of the decimated PCD image $\hat{I}_1^{(p)}(x_m + \Delta x, y_n)$ can be expressed as

$$\begin{aligned} &\hat{I}_1^{(p)}(x_m + \Delta x, y_n) \\ &= \hat{I}_1^{(p)}(x_m, y_n) e^{j2\pi f_{D_p}(y_n)\frac{\Delta x}{v}} \\ &- \int_0^{\frac{\Delta x}{v}} s_r(t + t_p + \frac{x_m}{v}) s^*(t + t_p + \frac{x_m}{v} \\ &- \frac{2\hat{r}_1(t + t_p, \Delta x, y_n)}{c}) e^{j\frac{4\pi}{\lambda}\hat{r}_1(t+t_p,\Delta x,y_n)} dt \\ &+ \int_0^{\frac{\Delta x}{v}} s_r(t + t_{p+1} + \frac{x_m}{v}) s^*(t + t_{p+1} + \frac{x_m}{v} \\ &- \frac{\hat{r}_1(t + t_{p+1}, \Delta x, y_n)}{c}) e^{j\frac{4\pi}{\lambda}\hat{r}_1(t+t_{p+1},\Delta x,y_n)} dt \\ &= \hat{I}_1^{(p)}(x_m, y_n) e^{j2\pi f_{D_p}(y_n)\frac{\Delta x}{v}} \\ &- e^{j\frac{4\pi}{\lambda}r(t_p,\Delta x,y_n)} \int_0^{\frac{\Delta x}{v}} s_r(t + t_p + \frac{x_m}{v}) s^*(t + t_p + \frac{x_m}{v} \\ &- \frac{2r(t_p, \Delta x, y_n)}{c}) dt \\ &+ e^{j\frac{4\pi}{\lambda}r(t_{p+1},\Delta x,y_n)} \int_0^{\frac{\Delta x}{v}} s_r(t + t_{p+1} + \frac{x_m}{v}) s^*(t + t_{p+1} \\ &+ \frac{x_m}{v} - \frac{2r(t_{p+1}, \Delta x, y_n)}{c}) dt. \end{aligned} \tag{26}$$

It is worthwhile noting that the zero-th order approximation is used in the decimated PCD imaging for reducing the complexity. It has nothing to do with PRI or slow time as in the conventional SAR imaging. The concept of PRI or slow time is no longer valid in any PCD imaging.

C. Decimated PCD Implementation

Assuming that each linear segment is further divided into K constant segments in the decimated PCD imaging, the imaging

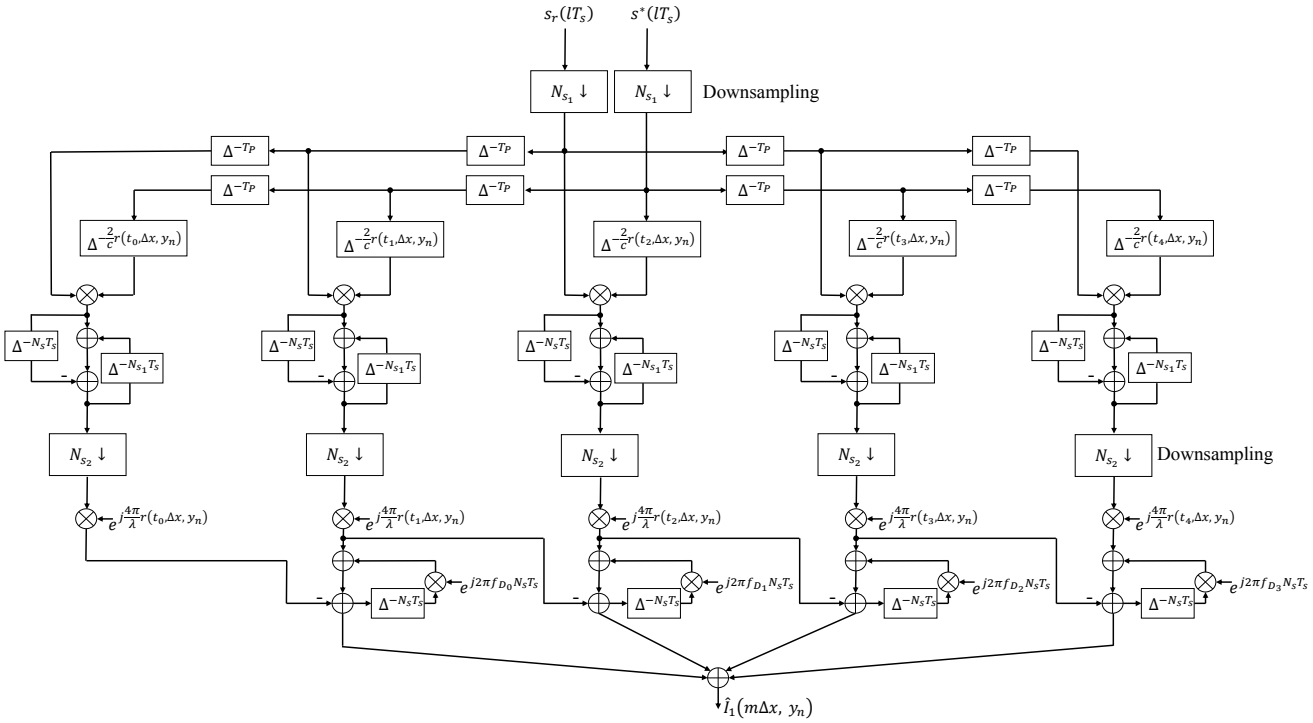

Fig. 5. Flow graph of decimated PCD algorithm for a given y_n, where $\Delta^{\pm\tau}$ denotes time delay or advance by τ, $l = i + mN_s$ denotes signal sampling time index, and m is the image azimuth sampling index.

spacing Δx can be extended from $T_s v$ to $(T_P v)/K = N_s T_s v$, where $N_s = T_P/(T_s K)$ is the number of received samples over each constant segment. The image azimuth coordinate can be expressed as $x_m = m\Delta x$ where m is an integer index describing the image pixel location in azimuth.

Replacing the integration over $[0, \Delta x/v)$ in (26) by a sum of N_s discrete signal samples, the recursive process can be expressed as

$$\begin{aligned}
&\hat{I}_1^{(p)}((m+1)\Delta x, y_n) \\
&= \hat{I}_1^{(p)}(m\Delta x, y_n) e^{j2\pi f_{D_p}(y_n) N_s T_s} - e^{j\frac{4\pi}{\lambda} r(t_p, \Delta x, y_n)} \\
&\cdot T_s \sum_{i=1}^{N_s} s_r((i+mN_s)T_s + t_p) s^*((i+mN_s)T_s + t_p \\
&- \frac{2r(t_p, \Delta x, y_n)}{c}) + e^{j\frac{4\pi}{\lambda} r(t_{p+1}, \Delta x, y_n)} T_s \sum_{i=1}^{N_s} s_r((i+mN_s)T_s \\
&+ t_{p+1}) s^*((i+mN_s)T_s + t_{p+1} - \frac{2r(t_{p+1}, \Delta x, y_n)}{c}).
\end{aligned} \tag{27}$$

Furthermore, the received and reference signals can be downsampled by a factor N_{s_1}. Hence, the number of samples involved in the summations can be reduced to $N_{s_2} = \frac{N_s}{N_{s_1}}$ and Eq. (27) can be further expressed as

$$\begin{aligned}
&\hat{I}_1^{(p)}((m+1)\Delta x, y_n) \\
&= \hat{I}_1^{(p)}(m\Delta x, y_n) e^{j2\pi f_{D_p}(y_n) N_s T_s} - e^{j\frac{4\pi}{\lambda} r(t_p, \Delta x, y_n)} N_{s_1} T_s \\
&\cdot \sum_{i=1}^{N_{s_2}} s_r((i+mN_{s_2})N_{s_1}T_s + t_p) s^*((i+mN_{s_2})N_{s_1}T_s \\
&+ t_p - \frac{2r(t_p, \Delta x, y_n)}{c}) + e^{j\frac{4\pi}{\lambda} r(t_{p+1}, \Delta x, y_n)} N_{s_1} T_s \sum_{i=1}^{N_{s_2}} s_r((i \\
&+ mN_{s_2})N_{s_1}T_s + t_{p+1}) s^*((i+mN_{s_2})N_{s_1}T_s + t_{p+1} \\
&- \frac{2r(t_{p+1}, \Delta x, y_n)}{c})
\end{aligned} \tag{28}$$

where the number of complex multiplications are reduced by N_{s_1} times. However, this simplification leads to a trade-off between Signal-to-Noise-Ratio (SNR) and complexity in the decimated PCD imaging since the downsampling reduces the SNR due to fewer samples of received signals being used. Hence, a proper selection of N_{s_1} and N_{s_2} should be made to suit a practical SAR application scenario.

Taking $P = 4$ as an example, the flow graph of the decimated PCD algorithm is drawn based on (28) as shown in Fig. 5, where the two summations in (28) and the two steps in the recursive imaging, i.e., adding and removing the respective summations, are achieved by the feedback loops in the middle and bottom of the flowchart respectively. Obviously, after extending the image spacing in azimuth by N_s times, the computational cost is largely reduced compared

with the original PCD algorithm which is the special case of $N_s = 1$.

D. Motion Compensation Strategy

In conventional Fourier-based SAR imaging, the range and azimuth compressions are performed in the fast and slow time dimensions respectively, where the two-dimensional FFT requires a uniform spatial sampling in azimuth. Therefore, the MOCO in cross-track and along-track motions must be considered. However, the PCD algorithm is a recursive imaging process in the time domain only, where the time-domain correlation does not require a uniform spatial sampling in azimuth. Therefore, the motion error will not deteriorate the imaging performance as long as the movement of the radar platform is known. In this subsection, a novel MOCO method well suited for the GCW-SAR data processing is proposed. How to mitigate the error caused by the dynamic nature of the targets is also addressed.

Assuming that the actual trajectory of the radar is set to $(x_r(t), y_r(t), h_r(t))$, the actual distance between the radar and the target can be described as

$$\begin{aligned} &r_a(t, x_m, y_n) = \sqrt{(y_r(t) + y_n)^2 + (x_m - x_r(t))^2 + h_r^2(t)} \\ &= \sqrt{R_r^2(t, y_n) + (x_m - x_r(t))^2} \end{aligned} \tag{29}$$

where $R_r(t, y_n) = \sqrt{(y_r(t) + y_n)^2 + h_r^2(t)}$. The MOCO strategies in range and azimuth imaging are presented as follows:

1) *MOCO in Range:* GCW-SAR distinguishes the range targets by the time delay of the received signal and the range imaging can be achieved via the time correlation between the received signal and the location-dependent reference signal. Hence, given $r_a(t, x_m, y_n)$, the reference signal $s^*(t - \frac{2r_a(t,x_m,y_n)}{c}) e^{j\frac{4\pi}{\lambda} r_a(t,x_m,y_n)}$ can be generated from the known transmitted signal $s(t)$ based on the actual trajectory of the radar to compensate the motion error.
2) *MOCO in Azimuth:* The PCD algorithm can tackle the non-uniform spatial sampling in azimuth by replacing the time correlation in (26) with the spatial correlation. Due to the non-uniform spatial sampling in azimuth, the number of the received samples in each linear/constant segment varies. Assuming that $N_s(m)$ samples are received when the moving platform travels over the m-th Δx and the corresponding downsampled factor is set to $N_{s_1}(m) = \frac{N_s(m)}{N_{s_2}(m)}$, the decimated PCD implementation can be derived as

$$\begin{aligned} &\hat{I}_1^{(p)}((m+1)\Delta x, y_n) \\ &= \hat{I}_1^{(p)}(m\Delta x, y_n) e^{j2\pi f_{D_p}(y_n)\frac{\Delta x}{v}} - e^{j\frac{4\pi}{\lambda} r_a(t_p(m), \Delta x, y_n)} \\ &\cdot N_{s_1}(m) T_s \sum_{i=1}^{N_{s_2}(m)} s_r(i \cdot N_{s_1}(m) T_s + \sum_{j=0}^{m} N_s(j) T_s \\ &+ t_p(m)) s^*(i \cdot N_{s_1}(m) T_s + \sum_{j=0}^{m} N_s(j) T_s + t_p(m) \\ &- \frac{2r_a(t_p(m), \Delta x, y_n)}{c}) + e^{j\frac{4\pi}{\lambda} r_a(t_{p+1}(m), \Delta x, y_n)} N_{s_1}(m) T_s \\ &\cdot \sum_{i=1}^{N_{s_2}(m)} s_r(i \cdot N_{s_1}(m) T_s + \sum_{j=0}^{m} N_s(j) T_s + t_{p+1}(m)) \\ &\cdot s^*(i \cdot N_{s_1}(m) T_s + \sum_{j=0}^{m} N_s(j) T_s + t_{p+1}(m) \\ &- \frac{2r_a(t_{p+1}(m), \Delta x, y_n)}{c}) \end{aligned} \tag{30}$$

where $t_p(m)$ stands for the time instant when the radar platform is located at the start point of p-th linear segment corresponding to the imaging point $(m\Delta x, y_n)$, and the compensation for the constant Doppler frequency shift is the same as that in (28). The cross-track motion error can be easily compensated based on the actual radar trajectory, and the two integrals in (26) can be calculated by the summation of the non-uniform spatial samples over the distance intervals $(x_r(t_p(m) + \sum_{j=0}^{m} N_s(j)T_s), x_r(t_p(m) + \sum_{j=0}^{m} N_s(j)T_s) + \Delta x]$ and $(x_r(t_{p+1}(m) + \sum_{j=0}^{m} N_s(j)T_s), x_r(t_{p+1}(m) + \sum_{j=0}^{m} N_s(j)T_s) + \Delta x]$ respectively, in which $x_r(t_p(m) + \sum_{j=0}^{m} N_s(j)T_s)$ denotes the radar location in azimuth at the start point of the p-th linear segment.

Compared with the decimated PCD imaging without MOCO strategy in (28), we can see that the expression of $r_a(t, x_m, y_n)$ without any approximation is adopted in (30) and the computational cost is not increased any more, resulting in an accurate and low-complexity MOCO strategy. On the contrary, most conventional SARs can only compensate for the first and second order components of the motion error due to the two-dimensional FFT operation and the MOCO processes also incur extra computational costs.

E. Decimated PCD Imaging Performance

The error function of the decimated PCD imaging can be also derived. Assuming that the time interval over the k-th constant segment of the p-th linear segment as shown in Fig. 4 (a) is described as $[t_p + \frac{x_m}{v} + k\frac{\Delta x}{v}, t_p + \frac{x_m}{v} + (k+1)\frac{\Delta x}{v})$ where $k = 0, 1, ..., K-1$, the approximated slant range $\hat{r}_1(t, x_m, y_n)$ can be expressed as

$$\begin{aligned} &\hat{r}_1(t, x_m, y_n) = \widetilde{r}_1(t_p + \frac{x_m}{v} + k\frac{\Delta x}{v}, x_m, y_n), \\ &t \in [t_p + \frac{x_m}{v} + k\frac{\Delta x}{v}, t_p + \frac{x_m}{v} + (k+1)\frac{\Delta x}{v}). \end{aligned} \tag{31}$$

The error in slant range caused by decimated PCD can be then expressed as

$$\begin{aligned}
&\hat{d}_1(t,x_m,y_n) = \hat{r}_1(t,x_m,y_n) - r(t,x_m,y_n)\\
&= \frac{r(t_{p+1},0,y_n) - r(t_p,0,y_n)}{(t_{p+1}-t_p)}(t_p + \frac{x_m}{v} + k\frac{\Delta x}{v} - t_p - \frac{x_m}{v})\\
&+ r(t_p,0,y_n) - r(t,x_m,y_n)\\
&\approx \frac{v^2(t_{p+1}+t_p)}{2R(y_n)}k\frac{\Delta x}{v} + \frac{v^2}{2R(y_n)}(t_p^2 - (t-\frac{x_m}{v})^2),\\
&t \in [t_p + \frac{x_m}{v} + k\frac{\Delta x}{v}, t_p + \frac{x_m}{v} + (k+1)\frac{\Delta x}{v}).
\end{aligned} \tag{32}$$

Similar to (19), the normalized error of decimated PCD imaging compared with the ideal matched filtering method can be evaluated as

$$\epsilon^2 = \frac{\int_{-\infty}^{\infty} |\hat{I}_1(x_m,0) - I(x_m,0)|^2 dx_m}{\int_{-\infty}^{\infty} |I(x_m,0)|^2 dx_m} \tag{33}$$

where $I(x_m,0)$ is expressed as (20). With the same technique used to derive (22), Eq (33) can be further expressed as

$$\begin{aligned}
\epsilon^2 &= \frac{\int_{-\infty}^{\infty} |rect(\frac{t}{T})(e^{j\frac{4\pi}{\lambda}\hat{d}_1(t,0,0)} - 1)|^2 dt}{\int_{-\infty}^{\infty} |rect(\frac{t}{T})|^2 dt}\\
&= \frac{\int_{-\frac{T}{2}}^{\frac{T}{2}} |e^{j\frac{4\pi}{\lambda}\hat{d}_1(t,0,0)} - 1|^2 dt}{\int_{-\frac{T}{2}}^{\frac{T}{2}} |1|^2 dt}\\
&= \frac{1}{T}\int_{-\frac{T}{2}}^{\frac{T}{2}} (e^{j\frac{4\pi}{\lambda}\hat{d}_1(t,0,0)} - 1)(e^{-j\frac{4\pi}{\lambda}\hat{d}_1(t,0,0)} - 1) dt\\
&= 2 - \frac{1}{T}\int_{-\frac{T}{2}}^{\frac{T}{2}} e^{j\frac{4\pi}{\lambda}\hat{d}_1(t,0,0)} dt - \frac{1}{T}\int_{-\frac{T_P}{2}}^{\frac{T}{2}} e^{-j\frac{4\pi}{\lambda}\hat{d}_1(t,0,0)} dt\\
&= 2 - 2Re\{\frac{1}{T}\int_{-\frac{T}{2}}^{\frac{T}{2}} e^{j\frac{4\pi}{\lambda}\hat{d}_1(t,0,0)} dt\}\\
&= 2 - 2Re\{\frac{1}{P}\sum_{p=0}^{P-1}\sum_{k=0}^{K-1} e^{j\frac{2\pi}{P^2}\frac{L}{L_a}((-P+2p+1)\frac{k}{K} + (-\frac{P}{2}+p)^2)}\\
&\cdot \sqrt{\frac{P^2}{2\pi}\frac{L_a}{L}}\Big(C((-\frac{P}{2}+p+\frac{k+1}{K})\sqrt{\frac{2\pi}{P^2}\frac{L}{L_a}})\\
&- C((-\frac{P}{2}+p+\frac{k}{K})\sqrt{\frac{2\pi}{P^2}\frac{L}{L_a}})\\
&+ jS((-\frac{P}{2}+p+\frac{k}{K})\sqrt{\frac{2\pi}{P^2}\frac{L}{L_a}})\\
&- jS((-\frac{P}{2}+p+\frac{k+1}{K})\sqrt{\frac{2\pi}{P^2}\frac{L}{L_a}})\Big)\}
\end{aligned} \tag{34}$$

where the closed-form expression of the integral $\frac{1}{T}\int_{-\frac{T}{2}}^{\frac{T}{2}} e^{j\frac{4\pi}{\lambda}\hat{d}_1(t,0,0)} dt$ is derived in Appendix C. We see that the decimated PCD error is a function of P, K and L/L_a.

Since $\hat{d}_1 \approx d_1$ when K is sufficiently large, the decimated PCD imaging error is bounded by the PCD imaging error. Therefore, in a practical GCW-SAR system, the GCW-SAR parameters L, L_a and P should firstly be determined to satisfy the upper bound of the GCW-SAR imaging performance. With the knowledge of P and L/L_a, K can then be selected based on (34) to meet the required imaging performance.

F. Complexity

For simplicity, the same observed scene is reconstructed by using PCD and decimated PCD algorithm respectively. It is also assumed that there are N^2 samples within a sweep of the observed area and the number of range pixels is N.

The PCD algorithm updates the image in azimuth recursively whenever the system obtains a new demodulated sample, thus achieving an $N \times N^2$ pixel image over the observed scene. Each image point in azimuth needs $3P+2$ complex multiplications [26], and thus the PCD algorithm requires $(3P+2) \times N^3$ complex multiplications.

However, after extending the azimuth imaging spacing, the decimated PCD algorithm only achieves an $N \times N^2/N_s$ pixel image and only uses part of the samples when $N_{s_1} > 1$, thus the computational cost is largely reduced. As seen in Fig. 5, the number of samples in azimuth has been reduced to N^2/N_{s_1} after the first downsampling, hence the decimated PCD algorithm only requires $(P+1)\cdot N \cdot N^2/N_{s_1}$ complex multiplications before the second downsampling. After the second downsampling, the recursion needs further $(2P+1)N^3/N_s$ complex multiplications. Therefore, the total computational complexity can be finally reduced to $(P+1)\cdot N^2 \cdot N/N_{s_1} + (2P+1)N^3/N_s$.

IV. Simulation Results

To compare the performance of different imaging algorithms, the same airborne simulation scenario is assumed. The transmitted signal is a continuous-wave periodic chirp signal. The SARs operate in the same stripmap mode with the following airborne SAR parameters [22]: carrier frequency $f_c = 10$ GHz, platform altitude $h_0 = 7000$ m, antenna aperture $L_a = 0.9$ m, speed of radar platform $v = 70$ m/s, and $R_c = 8082.9$ m. To present the imaging performance in azimuth clearly, the y coordinate is normalized by the azimuth resolutions $\delta_x = \frac{L_a}{2}$ in the first four simulation experiments.

A. Comparison between Conventional SAR imaging and PCD imaging

In the first simulation experiment, we compare the performance of an FMCW-SAR using PCD algorithm and range Doppler algorithm respectively assuming that the number of linear segments, P, is the same as the number of PRIs, N, over a synthetic aperture time. Due to the zero-th order approximation of the slant range for the conventional range Doppler algorithm, azimuth ambiguity will occur if the PRI is large. However, the azimuth ambiguity using the PCD algorithm can be greatly reduced due to the first order approximation even if the linear segment is long. With the radar parameters given at the beginning of this section, the length of the synthetic aperture is almost $600\delta_x$, and the lowest bound of the unambiguous pulse repetition frequency (PRF), i.e., 1/PRI, is $78Hz$. Fig. 6 shows the imaging performance of a one-point image at $(0,0)$ with $N = P = 250$ and $N = P = 100$ respectively. Obviously, the first order approximation in PCD

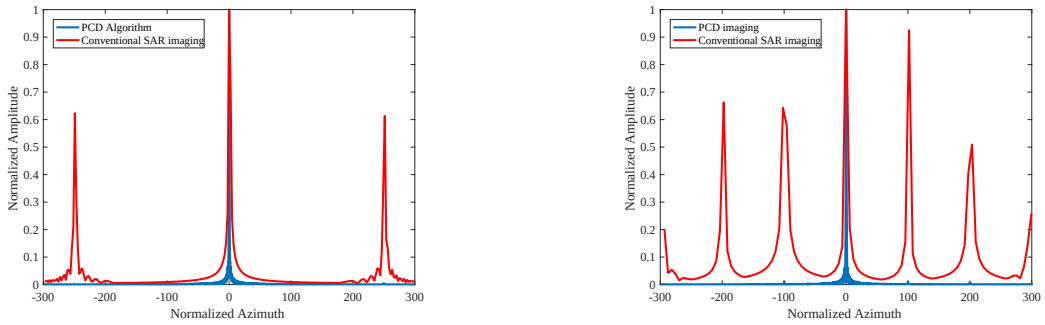

Fig. 6. Comparison between PCD imaging and conventional SAR imaging when $N = P < 300$: (a) $P = N = 250$; (b) $P = N = 100$.

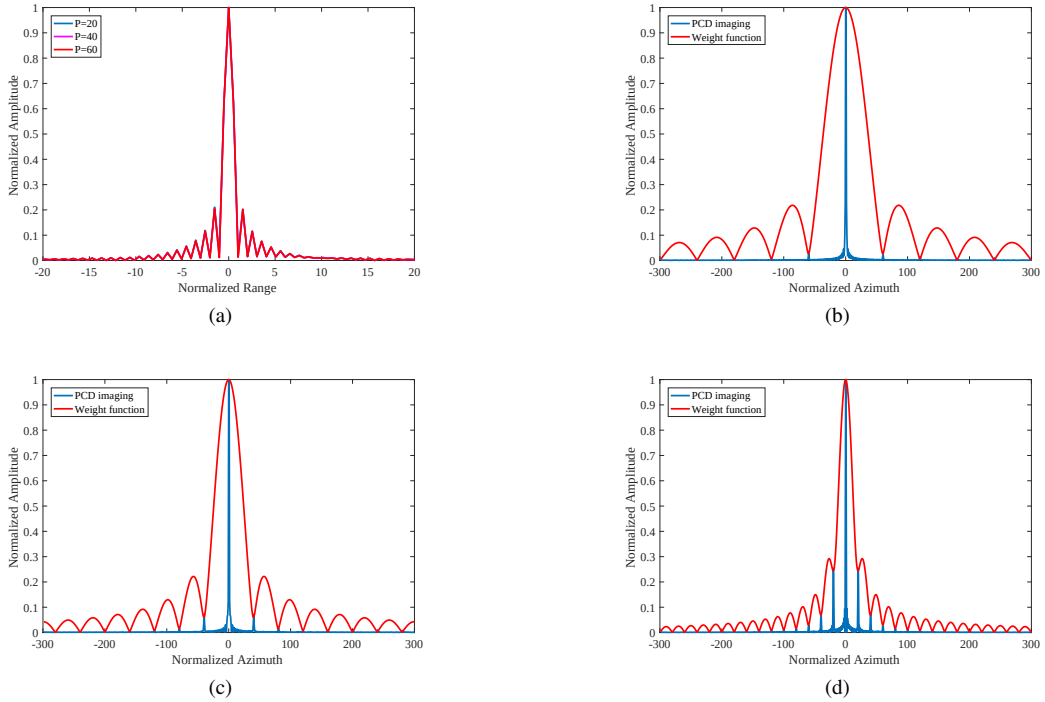

Fig. 7. PCD images in range and azimuth respectively, where the range images with $P = 60$, 40 and 20 are shown in (a), and the azimuth images and corresponding weight function $|W(x)|$ with different P are shown in (b) $P = 60$ ($Q = 12$), (c) $P = 40$ ($Q = 5.33$), and (d) $P = 20$ ($Q = 1.33$) respectively.

imaging can reduce the azimuth ambiguity caused by the inadequate PRF in conventional SAR. In Fig. 6 (a), the first azimuth ambiguity will appear at the points $x = 250\delta_x$ and $x = -250\delta_x$ symmetrically when $N = P = 250$. Such ambiguities can be reduced to a negligible level in PCD imaging.

B. Performance of PCD Imaging

The PCD imaging performance theoretically derived in Section II is validated in the second simulation experiment. For simplicity, a one-point image at $(0, 0)$ is assumed. Firstly, we show the range images with $P = 60$, 40 and 20 respectively in Fig. 7 (a). We see that the change in P makes no difference to the range image quality since the slant range is much longer than the length of a linear segment. The azimuth images with $P = 60$, 40 and 20 are shown in Fig. 7 (b), (c) and (d) respectively, where the corresponding values of the image quality factor Q are 12, 5.33 and 1.33, respectively, with $L_a = 0.9$ m and $L \approx 270$ m. It is clearly seen that an azimuth image is a sum of a set of sinc functions spaced by $P\frac{L_a}{2}$. The corresponding weight function $|W(x)|$ are plotted with the red lines in the figures, noting that the $i \cdot P\frac{L_a}{2}, i = \pm 1, \pm 2, ...,$ are the locations of the local minimums of $|W(x)|$. The imaging performance shows that the ambiguity caused by PCD becomes increasingly negligible when $Q > 5.33$ and the corresponding $\epsilon^2 < 0.05$.

C. Performance of Decimated PCD Imaging

The decimated PCD algorithm further adopts the zero-th order approximation in each linear segment and thus can

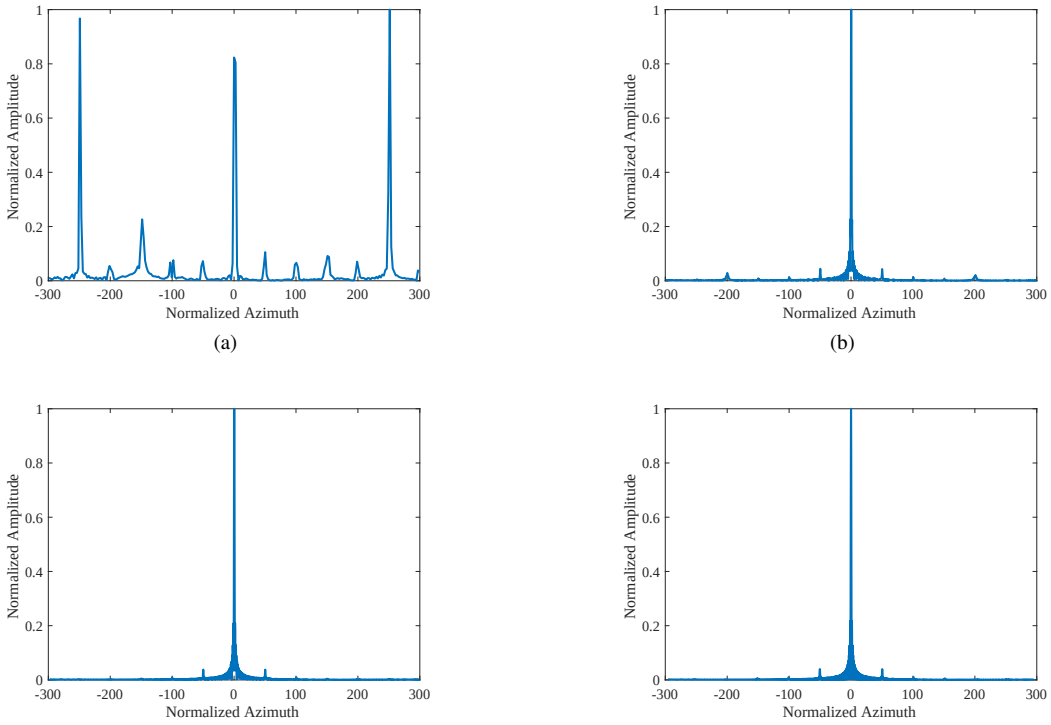

Fig. 8. Imaging performance of decimated PCD algorithm with different azimuth spacings: (a) $\Delta x = 1$ m ($K = 5$); (b) $\Delta x = 0.25$ m ($K = 20$); (c) $\Delta x = 0.125$ m ($K = 40$); and (d) $\Delta x = 0.025$ m ($K = 200$).

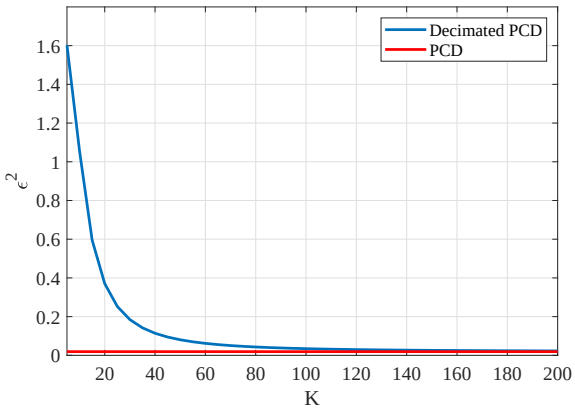

Fig. 9. Decimated PCD error as a function of K, when $P = 50$, $L/L_a = 300$ and $Q = 8.33$.

significantly reduce computational complexity. The azimuth image spacing Δx can be extended so that the redundant imaging points in the original PCD algorithm can be removed.

In this simulation experiment, the impact of azimuth image spacing Δx on the decimated PCD performance is investigated. Based on the aforementioned SAR parameters, the ratio L/L_a is 300. The number of linear segment P is set to 50 and the corresponding $Q = 8.33$. A one-point image at $(0, 0)$ is adopted and the azimuth imaging results with $\Delta x = 1$ m, 0.25 m, 0.125 m and 0.025 m (corresponding $K = 5, 20, 40$, and 200) are shown respectively in Fig. 8. It is evident that the azimuth ambiguity can be reduced with the decreasing Δx. Compared with the PCD error at $Q = 8.33$, the decimated PCD error as a function of K is shown in Fig. 9. We see that the PCD imaging error $\epsilon^2 = 0.02$ is the lower bound of the decimated PCD imaging. When K is larger than 140 ($\Delta x < 0.036$ m), the error caused by the zero-th order approximation can be neglected. In fact, K does not necessarily need to be reduced to 140 as Fig. 8 shows that almost the same imaging performance can be obtained when $K > 40$ since ϵ^2 is small enough. Therefore, a high-quality image with a large Δx can be achieved by decimated PCD imaging as long as ϵ^2 is sufficiently small.

D. Complexity and Impact of Downsampling on SNR

In the fourth simulation experiment, we compare the computational cost between PCD and decimated PCD algorithms and investigate the impact of downsampling on SNR in decimated PCD algorithm. With $P = 50$, $L/L_a = 300$, $T_s = 5 \times 10^{-9}$ s and $\Delta x = 0.125$ m ($K = 40$), a one-point image at $(0, 0)$ is reconstructed by PCD and decimated PCD algorithms respectively. The number of complex multiplications in PCD imaging can be computed as 1.17×10^{11}. In decimated PCD imaging, with $N_{s_1} = 10000, 1000, 100$, and 10 respectively, the number of complex multiplications can be reduced to 4.13×10^6, 3.95×10^7, 3.93×10^8 and 3.93×10^9 respectively. Hence, the computational cost is significantly reduced in the decimated PCD imaging. Although a larger N_{s_1} can achieve a lower computational complexity, it also leads to a lower SNR after image reconstruction. Assuming that the SNR in the receiver is

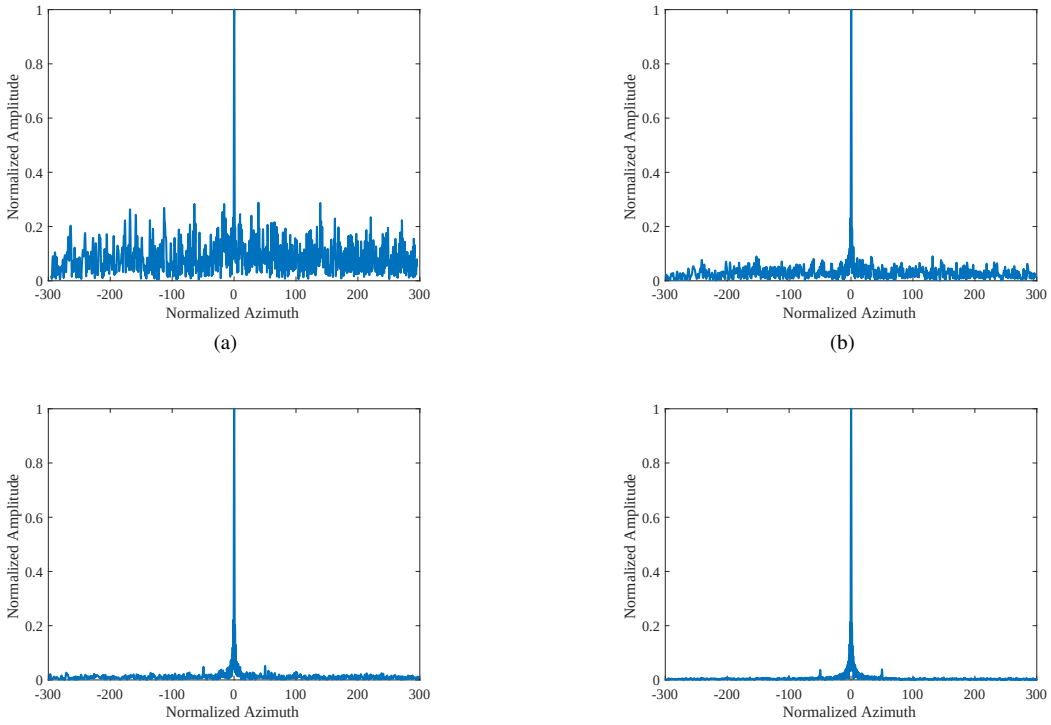

Fig. 10. Decimated PCD images in azimuth with different N_{s_1}: (a) $N_{s_1} = 10000$, (b) $N_{s_1} = 1000$, (c) $N_{s_1} = 100$ and (d) $N_{s_1} = 10$.

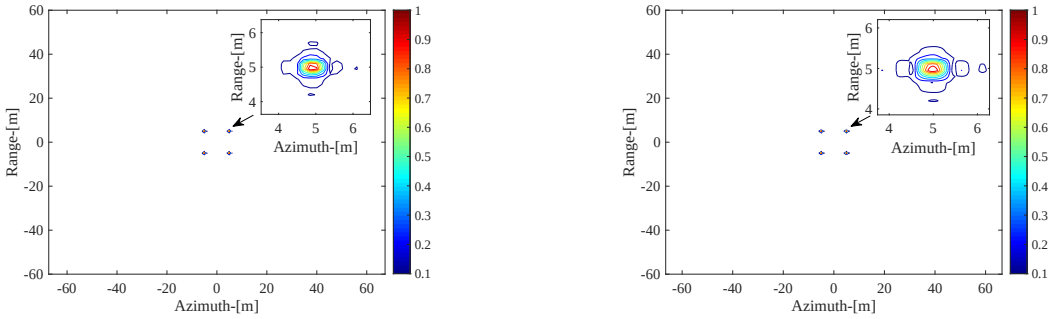

Fig. 11. Multi-targets SAR imaging comparison among different Δx: (a) $\Delta x = 0.18$ m ($K = 30$) and (b) $\Delta x = 0.027$ m ($K = 200$).

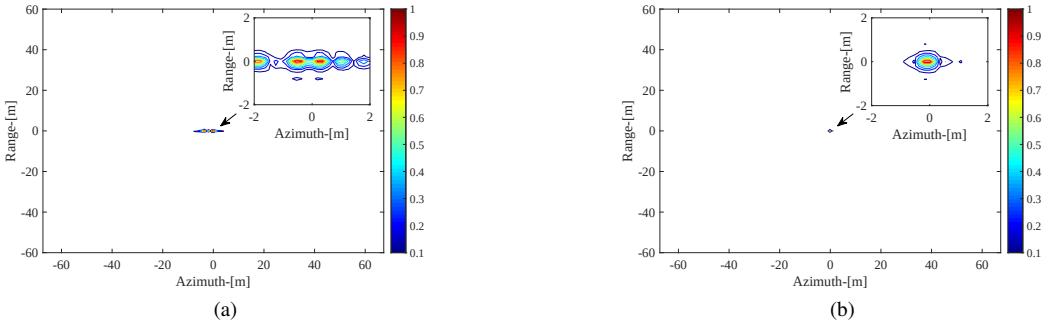

Fig. 12. Imaging performance of decimated PCD incorporated with MOCO strategy: (a) imaging without MOCO and (b) imaging with MOCO.

-30 dB, the final SAR images with $N_{s_1} = 10000, 1000, 100,$ and 10 are shown in Fig. 10 respectively, validating the

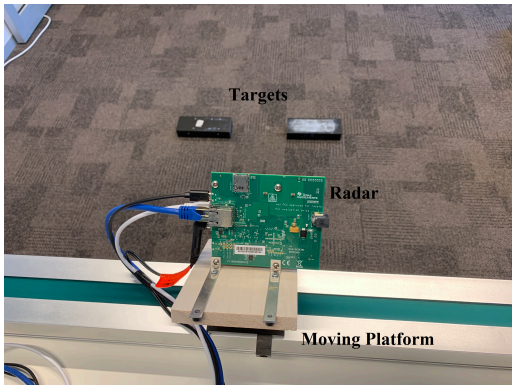

Fig. 13. Front view of the indoor GCW-SAR experimental scenario.

trade-off between complexity and SNR. Therefore, N_{s_1} and N_{s_2} should be determined appropriately to achieve a balance between SNR and complexity.

E. Decimated PCD Image with Multiple Targets

In the fifth simulation experiment, we compare the multiple-target decimated PCD imaging with different Δx. P is set to 50 and L/L_a is equal to 300 in the simulation. The transmitted signal bandwidth is set to 1 GHz and L_a is 0.9 m. The range and azimuth resolution are thus equal to 0.3 m and 0.45 m respectively. The final decimated PCD images with $\Delta x = 0.18$ m ($K = 30$) and $\Delta x = 0.027$ m ($K = 200$) are shown in Fig. 11 respectively. It is clearly seen that the error caused by the zero-th order approximation in decimated PCD algorithm is negligible with a proper Δx.

F. Effect of MOCO Strategy in PCD Imaging

In the final simulation experiment, the imaging performance of the decimated PCD implementation incorporated with the MOCO strategy is investigated. The speed of the radar platform is set to $v = v_0 + 3 \cdot sin(2\pi(v_0 t/L))$ m/s, where $v_0 = 70$ m/s. With $P = 50$, $L/L_a = 300$, and $\Delta x = 0.18$ m ($K = 30$), a point-target image at $(0, 0)$ is reconstructed by using the decimated PCD algorithms with and without MOCO respectively. We can see from Fig. 12 that the non-ideal radar trajectory deteriorates the decimated PCD imaging, but the motion error can be removed after applying the proposed MOCO strategy.

V. Experimental Results

In this section, we validate the proposed GCW-SAR parameter selection method and demonstrate the decimated PCD algorithm performance by using the real data received from a GCW-SAR experimental platform. For simplicity, an indoor GCW-SAR experimental environment is built with the following parameters: platform altitude $h_0 = 0.92$ m, synthetic aperture $L = 0.2$ m, speed of radar platform $v = 0.8$ m/s, and $R_c = 1.44$ m. The AWR1843 single-chip 77-GHz FMCW radar sensor made by Texas Instruments [30] is used as the radio front-end, where the carry frequency is 77 GHz and the bandwidth is set to 3.6 GHz to maximize the range resolution. Therefore, the range and azimuth resolutions of the GCW-SAR image are 0.0541 m and 0.0140 m respectively. The front view of the radar system is shown in Fig. 13, where the targets are two rectangular metal blocks with a size of 0.225 m $\times$ 0.08 m located at the center of the beam footprint. The received data stream is transferred to a personal computer and the PCD images are reconstructed by using MATLAB 2019.

With the known fixed L and L_a in the experimental scenario, the PCD image quality Q is only determined by the P. Based on the proposed GCW-SAR parameter design, to obtain the normalized PCD imaging error $\epsilon^2 = 0.1$, the image quality factor Q is approximately equal to 3.6 and thus P is set to 5. For comparison, the GCW-SAR images with different Q values $= 0.5617$, 3.5106, and 14.0425, corresponding to P$=$ 2, 5, and 10 respectively, are reconstructed by using the decimated PCD algorithm with the same $\Delta x = 0.004$ m, as shown in Fig. 14. It is evident that the two targets can be shown clearly in the GCW-SAR image with the $Q = 3.5106$. When Q is increased to 14.0425, the improvement of the image quality in azimuth can be hardly seen, and a small Q can lead to a worse PCD imaging performance. Therefore, $P = 5$ is suitable for this real imaging system.

Substituting $P = 5$ and $L/L_a = 7.1212$ into (34), the number of constant segments K in the decimated PCD algorithm can then be selected. Fig. 16 shows the relationship between K and ϵ^2. To keep $\epsilon^2 \leq 0.2$, K is set to 10. The real data GCW-SAR images reconstructed by using different $K = 2$, 5, and 10 are shown respectively with the same $P = 5$ and $L/L_a = 7.1212$ in Fig. 15. We can see that the two targets can be seen clearly even when $K = 5$ where the corresponding $\epsilon^2 = 0.4$ since the radar cross section of the targets is much higher than that of the carpet floor. Therefore, the threshold of ϵ^2 is determined based on the different imaging scenarios. In addition, the computational cost can be further reduced by downsampling the received signal. In the above experimental results, N_{s1} is set to 360, thus reducing the received signal sampling to 10 MHz. With the known $P = 5$, $L/L_a = 7.1212$, and $K = 10$, the real data GCW-SAR image with $N_{s1} = 720$ is reconstructed as shown in Fig. 17. With reduced SNR, the two targets cannot be distinguished and thus N_{s1} should be set to 360 in this GCW-SAR experimental scenario.

In summary, to design a practical GCW-SAR system, the antenna aperture L_a and the transmitted signal bandwidth should be firstly determined to ensure the azimuth and range resolutions. Then, the synthetic aperture L is obtained based on the carrier frequency and the imaging distance. With the known L/L_a ratio and the desired normalized PCD error ϵ^2, the number of linear segments P can be determined. Substituting P and L/L_a into (34), the number of constant segments K can be further determined. Finally, the N_{s1} can be selected based on the required SNR.

VI. Conclusion

Detailed analysis, further simplification and MOCO of the PCD algorithm are presented in this paper. Compared with the zero-th order approximation to the slant range in conventional SAR imaging, the PCD imaging demonstrates

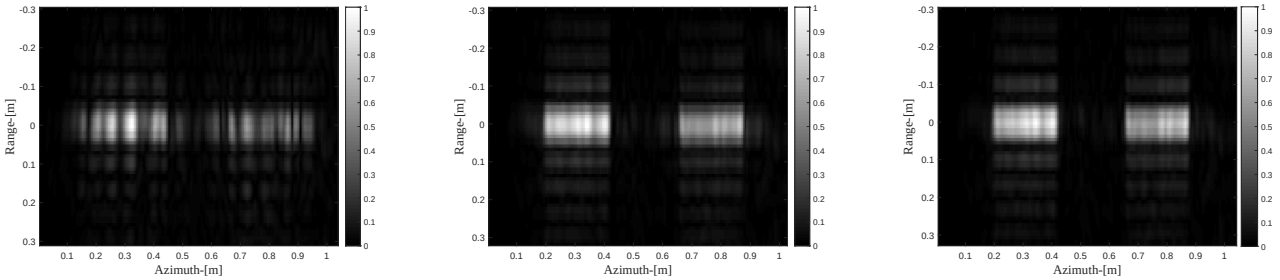

(a) (b) (c)

Fig. 14. Real data GCW-SAR imaging comparison among different Q: (a) Q= 0.5617, (b) Q= 3.5106, and (c) Q= 14.0425.

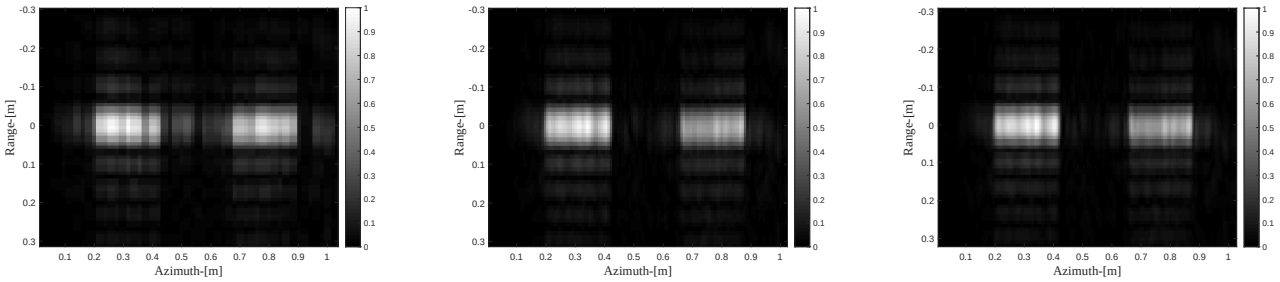

(a) (b) (c)

Fig. 15. Real data GCW-SAR imaging comparison among different K with the same $P = 5$ and $L/L_a = 7.1212$: (a) $K = 2$ ($\Delta x = 0.02$ m), (b) $K = 5$ ($\Delta x = 0.008$ m), and (c) $K = 10$ ($\Delta x = 0.004$ m).

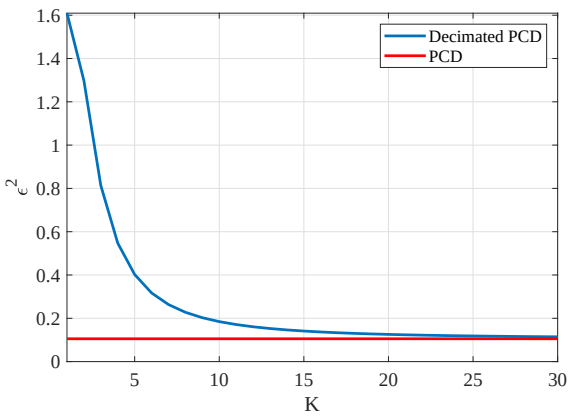

Fig. 16. Decimated PCD error function with different K, where $P = 5$ and $L/L_a = 7.1212$.

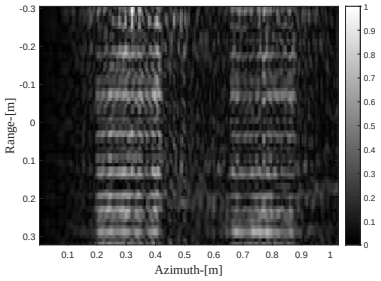

Fig. 17. Real data GCW-SAR image with the $N_{s1} = 720$.

many advantages due to the one-dimensional data structure and the first order approximation to the slant range. The closed form ambiguity functions in range and azimuth directions are derived respectively. With ideal matched filtering method as the benchmark, the normalized imaging error function of the PCD algorithm is also formulated, which can be defined as a function of the image quality factor. A simplified PCD algorithm, called decimated PCD algorithm, is also proposed, which can significantly reduce the imaging complexity with negligible degradation on imaging performance. The corresponding imaging error, lower-bounded by the PCD imaging error function, is also analyzed. To remove the imaging error caused by the non-ideal radar trajectory, a novel MOCO strategy well suited for the decimated PCD imaging is developed. The work presented in this paper and supported by the experimental results validates the theoretical foundation of the PCD algorithm in terms of imaging process, ambiguity function, performance bound, simplified implementation and MOCO, serving as a practical guideline to the GCW-SAR system design.

APPENDIX A
DERIVATION OF PCD AZIMUTH AMBIGUITY FUNCTION

Defining the rectangular function $rect(\frac{t}{T})$ as

$$rect(\frac{t}{T}) = \begin{cases} 1, & |t| < T/2, \\ \frac{1}{2}, & |t| = T/2, \\ 0, & \text{otherwise} \end{cases} \tag{35}$$

the PCD image $I_1(x_m,0)$ in (16) can be described as

$$\begin{aligned} &I_1(x_m,0)\\ &=\sigma(0,0)e^{-j\frac{2\pi x_m^2}{\lambda R_c}}\int_{-\infty}^{\infty}\frac{1}{T}rect(\frac{t}{T})e^{j\frac{4\pi}{\lambda}d_1(t,0,0)}\\ &\cdot e^{-j2\pi\frac{2vx_m}{\lambda R_c}t}dt \end{aligned} \tag{36}$$

which can be viewed as a Fourier transform, in terms of a frequency variable $\Omega=\frac{2vx_m}{\lambda R_c}$. The time domain function, which is a product of $\frac{1}{T}rect(\frac{t}{T})$ and $e^{j\frac{4\pi}{\lambda}d_1(t,0,0)}$, can be represented as a convolution in Ω domain, so that Eq. (36) can be rewritten as

$$\begin{aligned} &I_1(x_m,0)\\ &=\sigma(0,0)e^{-j\frac{2\pi x_m^2}{\lambda R_c}}\Big(\int_{-\infty}^{\infty}\frac{1}{T}rect(\frac{t}{T})e^{-j2\pi\Omega t}dt\\ &\otimes\int_{-\infty}^{\infty}e^{j\frac{4\pi}{\lambda}d_1(t,0,0)}e^{-j2\pi\Omega t}dt\Big) \end{aligned} \tag{37}$$

where $\otimes$ denotes convolution operation. The expression of $\frac{1}{T}rect(t)$ in Ω domain is the sinc function $sinc(T\Omega)$. Since $d_1(t,x_m,y_n)$ is a periodic function, the Fourier transform of $e^{j\frac{4\pi}{\lambda}d_1(t,0,0)}$ can be expressed as

$$\int_{-\infty}^{\infty}e^{j\frac{4\pi}{\lambda}d_1(t,0,0)}e^{-j2\pi\Omega t}dt=\frac{1}{T_P}\sum_{i=-\infty}^{\infty}D(\frac{i}{T_P})\delta(\Omega-\frac{i}{T_P}) \tag{38}$$

where $D(\Omega)$ is the Fourier transform of $e^{j\frac{4\pi}{\lambda}d_1(t,0,0)}$ in one period, i.e.,

$$D(\Omega)=\int_{-\frac{T_P}{2}}^{\frac{T_P}{2}}e^{j\frac{4\pi}{\lambda}d_1(t,0,0)}e^{-j2\pi\Omega t}dt. \tag{39}$$

Therefore, $I_1(x_m,0)$ can be expressed as

$$\begin{aligned} &I_1(x_m,0)\\ &=\sigma(0,0)e^{-j\frac{2\pi x_m^2}{\lambda R_c}}\Big(sinc(T\Omega)\otimes\frac{1}{T_P}\sum_{i=-\infty}^{\infty}D(\frac{i}{T_P})\delta(\Omega-\frac{i}{T_P})\Big)\\ &=\sigma(0,0)e^{-j\frac{2\pi x_m^2}{\lambda R_c}}\Big(\frac{1}{T_P}\sum_{i=-\infty}^{\infty}D(\frac{i}{T_P})sinc(T(\Omega-\frac{i}{T_P}))\Big). \end{aligned} \tag{40}$$

Defining $W(x)=\frac{1}{T_P}D(\frac{2vx}{\lambda R_c})$ and replacing Ω by $\frac{2vx}{\lambda R_c}$, we have the final expression of (16).

APPENDIX B
PCD WEIGHT FUNCTION

Assuming that the number of linear segments, P, is odd, $d_1(t,0,0)$ in the integration interval $[-\frac{T_P}{2},\frac{T_P}{2})$ can be expressed as

$$d_1(t,0,0)=\frac{v^2}{2R_c}(-t^2+\frac{T_P^2}{4}),t\in[-\frac{T_P}{2},\frac{T_P}{2}). \tag{41}$$

Hence, the corresponding weight function can be derived as

$$\begin{aligned} W(x)&=\frac{1}{T_P}\int_{-\frac{T_P}{2}}^{\frac{T_P}{2}}e^{j\frac{4\pi}{\lambda}d_1(t,0,0)}e^{-j2\pi\frac{2vx}{\lambda R_c}t}dt\\ &=\frac{1}{T_P}\int_{-\frac{T_P}{2}}^{\frac{T_P}{2}}e^{j\frac{4\pi}{\lambda}\frac{v^2}{2R_c}(-t^2+\frac{T_P^2}{4})}e^{-j2\pi\frac{2vx}{\lambda R_c}t}dt\\ &=e^{j\frac{\pi v^2T_P^2}{2\lambda R_c}}\frac{1}{T_P}\int_{-\frac{T_P}{2}}^{\frac{T_P}{2}}e^{-j\frac{2\pi}{\lambda R_c}(v^2t^2+2xvt)}dt\\ &=e^{j\frac{\pi v^2T_P^2}{2\lambda R_c}}e^{j\frac{2\pi x^2}{\lambda R_c}}\frac{1}{T_P}\int_{-\frac{T_P}{2}}^{\frac{T_P}{2}}e^{-j\frac{2\pi}{\lambda R_c}(vt+x)^2}dt\\ &=\sqrt{\frac{\lambda R_c}{2\pi v^2T_P^2}}e^{j\frac{\pi v^2T_P^2}{2\lambda R_c}}e^{j\frac{2\pi x^2}{\lambda R_c}}\int_{(x-\frac{T_P}{2}v)\sqrt{\frac{2\pi}{\lambda R_c}}}^{(x+\frac{T_P}{2}v)\sqrt{\frac{2\pi}{\lambda R_c}}}e^{-jt^2}dt\\ &=\sqrt{\frac{\lambda R_c}{2\pi v^2T_P^2}}e^{j\frac{\pi v^2T_P^2}{2\lambda R_c}}e^{j\frac{2\pi x^2}{\lambda R_c}}\Big(\int_0^{(x+\frac{T_P}{2}v)\sqrt{\frac{2\pi}{\lambda R_c}}}(cos(t^2)\\ &-jsin(t^2))dt-\int_0^{(x-\frac{T_P}{2}v)\sqrt{\frac{2\pi}{\lambda R_c}}}(cos(t^2)-jsin(t^2))dt\Big)\\ &=\sqrt{\frac{\lambda R_c}{2\pi v^2T_P^2}}e^{j\frac{\pi v^2T_P^2}{2\lambda R_c}}e^{j\frac{2\pi x^2}{\lambda R_c}}\Big(C((x+\frac{T_P}{2}v)\sqrt{\frac{2\pi}{\lambda R_c}})\\ &-C((x-\frac{T_P}{2}v)\sqrt{\frac{2\pi}{\lambda R_c}})+jS((x-\frac{T_P}{2}v)\sqrt{\frac{2\pi}{\lambda R_c}})\\ &-jS((x+\frac{T_P}{2}v)\sqrt{\frac{2\pi}{\lambda R_c}})\Big) \end{aligned} \tag{42}$$

where $S(x)$ and $C(x)$ are the Fresnel integrals respectively [29] defined as

$$\begin{aligned} S(x)&=\int_0^x sin(t^2)dt=\sum_{n=0}^{\infty}(-1)^n\frac{x^{4n+3}}{(2n+1)!(4n+3)},\\ C(x)&=\int_0^x cos(t^2)dt=\sum_{n=0}^{\infty}(-1)^n\frac{x^{4n+1}}{(2n)!(4n+1)}. \end{aligned} \tag{43}$$

Since $L\approx\frac{\lambda}{L_a}R_c$, Eq. (42) is further expressed as (17).

When P is even, $d_1(t,0,0)$ is a time $\frac{T_P}{2}$ shifted version of that with odd P, so that $W(x)$ has the same expression as (42) except for a phase shift $e^{-j\frac{2\pi vT_P}{\lambda R_c}x}$. Note that both weight functions have the same amplitude $|W(x)|$ and $W(0)$.

APPENDIX C
INTEGRAL IN DECIMATED PCD ERROR FUNCTION

Based on (34), the integral $\frac{1}{T}\int_{-\frac{T}{2}}^{\frac{T}{2}}e^{j\frac{4\pi}{\lambda}\hat{d}_1(t,0,0)}dt$ can be expressed as a sum of $P\cdot K$ integrations over respective

constant segments of the slant range, i.e.,

$$\begin{aligned}
&\frac{1}{T}\int_{-\frac{T}{2}}^{\frac{T}{2}} e^{j\frac{4\pi}{\lambda}\hat{d}_1(t,0,0)}dt \\
&= \frac{1}{T}\sum_{p=0}^{P-1}\sum_{k=0}^{K-1}\int_{t_p+k\frac{\Delta x}{v}}^{t_p+(k+1)\frac{\Delta x}{v}} e^{j\frac{4\pi}{\lambda}\frac{v^2(t_{p+1}+t_p)}{2R_c}k\frac{\Delta x}{v}+\frac{v^2}{2R_c}(t_p^2-t^2)}dt \\
&= \frac{1}{T}\sum_{p=0}^{P-1}\sum_{k=0}^{K-1}\int_{t_p+k\frac{\Delta x}{v}}^{t_p+(k+1)\frac{\Delta x}{v}} e^{j\frac{2\pi v^2}{\lambda R_c}(-t^2+(t_{p+1}+t_p)k\frac{\Delta x}{v}+t_p^2)}dt \\
&= \frac{1}{P}\sum_{p=0}^{P-1}\sum_{k=0}^{K-1} e^{j\frac{2\pi v^2}{\lambda R_c}((t_{p+1}+t_p)k\frac{\Delta x}{v}+t_p^2)}\sqrt{\frac{\lambda R_c}{2\pi v^2 T_P^2}} \\
&\cdot\int_{(t_p+k\frac{\Delta x}{v})\sqrt{\frac{2\pi v^2}{\lambda R_c}}}^{(t_p+(k+1)\frac{\Delta x}{v})\sqrt{\frac{2\pi v^2}{\lambda R_c}}} e^{-jt^2}dt.
\end{aligned} \tag{44}$$

Since $t_p = -\frac{T}{2}+pT_P$, $L \approx \frac{\lambda}{L_a}R_c$, and $\Delta x = \frac{T_P}{K}v$, Eq. (44) can be further derived as

$$\begin{aligned}
&\frac{1}{T}\int_{-\frac{T}{2}}^{\frac{T}{2}} e^{j\frac{4\pi}{\lambda}\hat{d}_1(t,0,0)}dt \\
&= \frac{1}{P}\sum_{p=0}^{P-1}\sum_{k=0}^{K-1} e^{j\frac{2\pi v^2}{\lambda R_c}((-T+(2p+1)T_P)k\frac{T_P}{K}+(-\frac{T}{2}+pT_P)^2)} \\
&\cdot\sqrt{\frac{\lambda R_c}{2\pi v^2 T_P^2}}\int_{(-\frac{T}{2}+pT_P+k\frac{T_P}{K})\sqrt{\frac{2\pi v^2}{\lambda R_c}}}^{(-\frac{T}{2}+pT_P+(k+1)\frac{T_P}{K})\sqrt{\frac{2\pi v^2}{\lambda R_c}}} e^{-jt^2}dt \\
&= \frac{1}{P}\sum_{p=0}^{P-1}\sum_{k=0}^{K-1} e^{j\frac{2\pi}{P^2}\frac{L}{L_a}((-P+2p+1)\frac{k}{K}+(-\frac{P}{2}+p)^2)} \\
&\cdot\sqrt{\frac{P^2}{2\pi}\frac{L_a}{L}}\int_{(-\frac{P}{2}+p+\frac{k}{K})\sqrt{\frac{2\pi}{P^2}\frac{L}{L_a}}}^{(-\frac{P}{2}+p+\frac{k+1}{K})\sqrt{\frac{2\pi}{Q}}} e^{-jt^2}dt \\
&= \frac{1}{P}\sum_{p=0}^{P-1}\sum_{k=0}^{K-1} e^{j\frac{2\pi}{P^2}\frac{L}{L_a}((-P+2p+1)\frac{k}{K}+(-\frac{P}{2}+p)^2)} \\
&\cdot\sqrt{\frac{P^2}{2\pi}\frac{L_a}{L}}\Big(C((-\frac{P}{2}+p+\frac{k+1}{K})\sqrt{\frac{2\pi}{P^2}\frac{L}{L_a}}) \\
&- C((-\frac{P}{2}+p+\frac{k}{K})\sqrt{\frac{2\pi}{P^2}\frac{L}{L_a}}) \\
&+ jS((-\frac{P}{2}+p+\frac{k}{K})\sqrt{\frac{2\pi}{P^2}\frac{L}{L_a}}) \\
&- jS((-\frac{P}{2}+p+\frac{k+1}{K})\sqrt{\frac{2\pi}{P^2}\frac{L}{L_a}})\Big).
\end{aligned} \tag{45}$$

ACKNOWLEDGMENT

This work was supported under the Australian Research Council (ARC) Discovery Project DP 160101693.

REFERENCES

[1] X. M. Li, S. Lehner, and T. Bruns, "Ocean Wave Integral Parameter Measurements Using Envisat ASAR Wave Mode Data," *IEEE Transactions on Geoscience and Remote Sensing*, vol. 49, no. 1, pp. 155–174, Jan 2011.

[2] J. H. Gonzalez, M. Bachmann, R. Scheiber, and G. Krieger, "Definition of ICESat Selection Criteria for Their Use as Height References for TanDEM-X," *IEEE Transactions on Geoscience and Remote Sensing*, vol. 48, no. 6, pp. 2750–2757, June 2010.

[3] J. P. Robin, M. Lafitte, and E. Coiras, "A review of SAR imagery exploitation methods in support of Defence and Security missions," in *Proceedings of EUSAR 2016: 11th European Conference on Synthetic Aperture Radar*, June 2016, pp. 1–5.

[4] A. Fiche, S. Angelliaume, L. Rosenberg, and A. Khenchaf, "Analysis of X-Band SAR Sea-Clutter Distributions at Different Grazing Angles," *IEEE Transactions on Geoscience and Remote Sensing*, vol. 53, no. 8, pp. 4650–4660, Aug 2015.

[5] C. H. Gierull and I. Sikaneta, "A Compound-Plus-Noise Model for Improved Vessel Detection in Non-Gaussian SAR Imagery," *IEEE Transactions on Geoscience and Remote Sensing*, vol. 56, no. 3, pp. 1444–1453, March 2018.

[6] A. Currie and M. A. Brown, "Wide-swath SAR," *IEE Proceedings F - Radar and Signal Processing*, vol. 139, no. 2, pp. 122–135, April 1992.

[7] M. Soumekh, *Synthetic aperture radar signal processing*. New York: Wiley, 1999, vol. 7.

[8] S. X. Zhang, M. D. Xing, X. G. Xia, L. Zhang, R. Guo, Y. Liao, and Z. Bao, "Multichannel HRWS SAR Imaging Based on Range-Variant Channel Calibration and Multi-Doppler-Direction Restriction Ambiguity Suppression," *IEEE Transactions on Geoscience and Remote Sensing*, vol. 52, no. 7, pp. 4306–4327, July 2014.

[9] Y. Shu, G. Liao, and Z. Yang, "Design Considerations of PRF for Optimizing GMTI Performance in Azimuth Multichannel SAR Systems With HRWS Imaging Capability," *IEEE Transactions on Geoscience and Remote Sensing*, vol. 52, no. 4, pp. 2048–2063, April 2014.

[10] L. B. Wang, D. W. Wang, J. J. Li, J. Xu, C. Xie, and L. Wang, "Ground Moving Target Detection and Imaging Using a Virtual Multichannel Scheme in HRWS Mode," *IEEE Transactions on Geoscience and Remote Sensing*, vol. 54, no. 9, pp. 5028–5043, Sept 2016.

[11] G. Krieger, N. Gebert, and A. Moreira, "Multidimensional Waveform Encoding: A New Digital Beamforming Technique for Synthetic Aperture Radar Remote Sensing," *IEEE Transactions on Geoscience and Remote Sensing*, vol. 46, no. 1, pp. 31–46, Jan 2008.

[12] N. Gebert, G. Krieger, and A. Moreira, "Digital Beamforming on Receive: Techniques and Optimization Strategies for High-Resolution Wide-Swath SAR Imaging," *IEEE Transactions on Aerospace and Electronic Systems*, vol. 45, no. 2, pp. 564–592, April 2009.

[13] J. Wang, X. D. Liang, L. Y. Chen, and K. Li, "A Novel Space-Time Coding Scheme Used for MIMO-SAR Systems," *IEEE Geoscience and Remote Sensing Letters*, vol. 12, no. 7, pp. 1556–1560, July 2015.

[14] W. Q. Wang, "Space-Time Coding MIMO-OFDM SAR for High-Resolution Imaging," *IEEE Transactions on Geoscience and Remote Sensing*, vol. 49, no. 8, pp. 3094–3104, Aug 2011.

[15] G. Krieger, "MIMO-SAR: Opportunities and Pitfalls," *IEEE Transactions on Geoscience and Remote Sensing*, vol. 52, no. 5, pp. 2628–2645, May 2014.

[16] W. Q. Wang, "MIMO SAR imaging: Potential and challenges," *IEEE Aerospace and Electronic Systems Magazine*, vol. 28, no. 8, pp. 18–23, Aug 2013.

[17] D. Bharadia, E. McMilin, and S. Katti, "Full Duplex Radios," *ACM SIGCOMM Computer Communication Review*, vol. 43, no. 4, pp. 375–386, 2013.

[18] A. Sabharwal, P. Schniter, D. Guo, D. W. Bliss, S. Rangarajan, and R. Wichman, "In-Band Full-Duplex Wireless: Challenges and Opportunities," *IEEE Journal on Selected Areas in Communications*, vol. 32, no. 9, pp. 1637–1652, Sept 2014.

[19] X. Huang and Y. J. Guo, "Radio Frequency Self-Interference Cancellation With Analog Least Mean-Square Loop," *IEEE Transactions on Microwave Theory and Techniques*, vol. 65, no. 9, pp. 3336–3350, Sep. 2017.

[20] J. Zhou, T. H. Chuang, T. Dinc, and H. Krishnaswamy, "Integrated Wideband Self-Interference Cancellation in the RF Domain for FDD and Full-Duplex Wireless," *IEEE Journal of Solid-State Circuits*, vol. 50, no. 12, pp. 3015–3031, Dec 2015.

[21] M. P. Chang, C. L. Lee, B. Wu, and P. R. Prucnal, "Adaptive Optical Self-Interference Cancellation Using a Semiconductor Optical Amplifier," *IEEE Photonics Technology Letters*, vol. 27, no. 9, pp. 1018–1021, May 2015.

[22] A. Meta, "Signal processing of FMCW Synthetic Aperture Radar Data," 2006.

[23] A. Meta, P. Hoogeboom, and L. P. Ligthart, "Signal Processing for FMCW SAR," *IEEE Transactions on Geoscience and Remote Sensing*, vol. 45, no. 11, pp. 3519–3532, Nov 2007.

[24] R. Wang, O. Loffeld, H. Nies, S. Knedlik, M. Hagelen, and H. Essen, "Focus FMCW SAR Data Using the Wavenumber Domain Algorithm," *IEEE Transactions on Geoscience and Remote Sensing*, vol. 48, no. 4, pp. 2109–2118, April 2010.

[25] Y. Liu, Y. K. Deng, and R. Wang, "Focus Squint FMCW SAR Data Using Inverse Chirp-Z Transform Based on an Analytical Point Target Reference Spectrum," *IEEE Geoscience and Remote Sensing Letters*, vol. 9, no. 5, pp. 866–870, Sept 2012.
[26] Y. Nan, X. Huang, and Y. J. Guo, "Generalized continuous wave synthetic aperture radar for high resolution and wide swath remote sensing," *IEEE Transactions on Geoscience and Remote Sensing*, pp. 1–13, 2018.
[27] ——, "A Generalized Continuous Wave Synthetic Aperture Radar," in *2017 IEEE 85th Vehicular Technology Conference (VTC Spring)*, June 2017, pp. 1–5.
[28] ——, "Passive synthetic aperture radar imaging with piecewise constant Doppler algorithm," in *2017 IEEE-APS Topical Conference on Antennas and Propagation in Wireless Communications (APWC)*, Sept 2017, pp. 41–44.
[29] J. Boersma, "Computation of Fresnel integrals," *Mathematics of Computation*, 1960.
[30] T. Instruments, "Awr1843 single-chip 77- and 79-ghz fmcw radar sensor," http://www.ti.com/lit/ds/swrs222/swrs222.pdf, Dec 2018, original document from Texas Instruments.